Supplementary Information

Highly spontaneous spin polarization engineering of single-atom artificial antioxidases towards efficient ROS elimination and tissue regeneration

Bihui Zhu,[a,1] Zhenyang Zhao,[b,1] Sujiao Cao,[a,*] Yimin Sun,[c] Liyun Wang,[a] Songya Huang,[a] Chong Cheng,[b] Lang Ma,[a,*] Li Qiu[a,*]

[a] Department of Medical Ultrasound, National Clinical Research Center for Geriatrics, West China Hospital, Sichuan University, Chengdu, 610041, China

[b] College of Polymer Science and Engineering, State Key Laboratory of Polymer Materials Engineering, Sichuan University, Chengdu, 610065, China

[c] West China Hospital of Stomatology, Sichuan University, Chengdu, 610041, China

[1]B.H. Zhu and Z.Y. Zhao contributed equally to this work.

* Corresponding authors. Email: caosujiao@163.com (S.J. Cao), malang1989@scu.edu.cn (L. Ma), and qiulihx@scu.edu.cn (L. Qiu).

Characterizations

Scanning electron microscopy (SEM) images were recorded on an Apreo S HiVoc (Thermo Fisher Scientific, FEI). Transmission electron microscopy (TEM) images and the corresponding mapping were obtained via a Talos F200x TEM microscope (FEI Ltd., USA) operated at 200 kV. A JEM-ARM200F transmission electron microscope (JEOL Ltd., Japan) operated at 200 kV, equipped with a probe spherical aberration corrector, was used to obtain the aberration-corrected high-angle annular dark-field scanning TEM (AC HAADF-STEM) images. N_2 sorption analysis was conducted on a TriStar 3020-accelerated surface area and porosimetry instrument, equipped with automated surface area, at 77 K using Brunauer-Emmett-Teller (BET) calculations for the surface area and pore diameter distribution. Raman spectra were performed on an inVia plus laser Raman confocal spectrometer (Renishaw Ltd., UK). XRD pattern presented the crystal phase state via a Bruker D8 Focus X-ray diffractometer with Cu radiation at a voltage of 40 kV. X-ray photoelectron spectroscopy (XPS) spectra were collected using a K-Alpha™+ X-ray Photoelectron Spectrometer System (Thermo Scientific, USA) with a Hemispheric 180° dual-focus analyzer (128-channel detector and monochromatic Al Kα irradiation).

X-ray absorption spectroscopy measurements

X-ray absorption spectra (XAS) were collected on the beamline BL07A1 in NSRRC (National Center for Synchrotron Radiation Research). The radiation was scanned by a Si(111) double-crystal monochromator. XAFS data was processed in Athena (version 0.9.26) for background, pre-edge line, and post-edge line calibrations. EXAFS spectra were fitted in a Fourier-transform using the metal phthalocyanine structure with an $M–N_4$ unit as the reference. The amplitude reduction factor (S_0^2) was set to 0.700, 0.740, and 0.795 during the fitting for Fe-AAO, Co-AAO, and Ni-AAO, respectively. X-ray absorption near-edge structure (XANES) and extended X-ray absorption fine structure spectra (EXAFS) data reduction and analysis were processed by Athena software. Wavelet Transform analysis was obtained by importing the $\chi(k)$ exported from Athena into the Hama Fortran code.

Cell culture

The human mesenchymal stem cells (hMSCs) were obtained from Cyagen (HUXMA-

01001), and cultured in hMSCs culture medium (Cyagen, HUXMA-90011) supplemented with 10% fetal bovine serum and 1% penicillin-streptomycin at 37 °C with 5% CO_2.

***In vitro* cytotoxicity evaluation of FA-AAO biocatalysts**

The cytotoxicity of FA-AAO biocatalysts was determined by the Cell Counting Kit-8 (CCK-8) assay *in vitro*. Briefly, hMSCs were seeded into 96-well culture plates at the density of 1×10^4 cells/well and incubated at 37 °C in an incubator with 5% CO_2 for 24 h. Afterward, the cell culture medium was aspirated, and fresh culture media containing Fe-AAO and Co-AAO (1 μg/mL) were added. After 24 h incubation, cells were gently washed once with sterile PBS and then treated with 100 μL fresh culture medium and CCK-8 solution and further incubated at 37 °C for 2 h. The cell viability was then quantified by measuring the absorbance value at 450 nm by a microplate reader (EON, BioTek, USA).

***In vitro* cytoprotective ability of FA-AAO biocatalysts**

To investigate the ROS scavenging ability of FA-AAO biocatalysts in cells, hMSCs were seeded into 96-well plates at the density of 1×10^4 cells per well. After 24 h incubation, FA-AAO with concentrations of 1 μg/mL was added to each group of wells and incubated for 24 h. Then, cells were treated with 100 μM H_2O_2 and further incubated at 37 °C for 2 h. After stimulation with H_2O_2, the cells were incubated with CCK-8. Furthermore, the live/dead cell viability assay was also carried out to evaluate the cytoprotective ability. Cells were stained at room temperature for 30 min by the propidium iodide (PI) and Hoechst 33342 working solution. After washing with PBS, the cells were observed under the fluorescence microscope (Olympus BX63, Japan) and subjected to a Celigo Image Cytometer (Nexcelom Bioscience, USA) for quantitative analysis. Cells without the addition of H_2O_2 were regarded as the negative control.

JC-1, a sensitive fluorescent probe, was extensively used to detect the mitochondrial membrane potential for cell apoptosis. In brief, after the abovementioned incubation with H_2O_2 for 2 h, cells were stained with the JC-1 working solution as protocol. The cells were washed with PBS three times and analyzed using flow cytometry (BECKMAN COULTER, USA).

2′,7′-Dichlorofluorescin diacetate (DCFH-DA, D6883, Sigma-Aldrich, USA) DCFH-DA was used to detect the intracellular ROS levels. With the same process as JC-1 staining, DCFH-DA was added to the treated cells and incubated in the dark at 37 °C for 30 min. Afterward, the

cells were washed, removing unloaded DCFH-DA dye. The intracellular ROS levels were monitored using a confocal laser scanning microscope (CLSM, Olympus FV1000, Japan) and semi-quantitatively analyzed by ImageJ.

Cell adhesion and osteogenic differentiation

To determine the effects of ROS and biocatalysts on cell adhesion behavior, cells treated with biocatalysts and H_2O_2 were washed once with cell culture medium and twice with PBS before fixation with 4% paraformaldehyde at room temperature for 10 minutes, followed by adding 0.1% Triton X-100 in PBS into fixed cells for 5 to 10 minutes to increase permeability. After rinsing the cells 3 times with PBS, cells were stained using Alexa Fluor 647 Conjugated Paxillin Antibody (Signalway Antibody, USA) and F-Actin Labeling Kit (Sangon Biotech, China) according to the manufacturer's instructions. Then, the nucleus was stained with DAPI at room temperature for half hour, followed by washing 3 times with PBS. Immunofluorescence images were acquired on an Olympus FV1000 CLSM and analyzed by Image J.

To investigate the effect of ROS and biocatalysts on cell differentiation, the treated hMSCs were seeded at a density of 1×10^4 cells/well on substrates of interest in osteogenic-induced media (Cyagen, HUXMX-90021). The medium was replaced every 3 days. Alkaline phosphatase (ALP) was utilized as a biomarker of osteogenic differentiation and was stained with BCIP/NBT (Beyotime, China) solution according to the manufacturer's instructions. Stained cells were observed in a microscope mounted with a color camera (Olympus BX63, Japan). The quantitative evaluation of ALP was performed using the BCA Protein Assay kit (Beyotime, China) based on the manufacturer's protocol, followed by measuring the absorbance value at 562 nm with a microplate reader.

Animal surgical procedure and *in vivo* therapy

All the procedures regarding animal maintenance and experiments were approved by the animal ethical standard from Animal Ethics Committee in West China Hospital, Sichuan University, Chengdu, China (2021164A). Each SD rat aged 8 weeks weighing between 300 and 350 g was randomly assigned to one of four groups (n = 3 per group). Surgical procedures were carried out under 2% isoflurane inhalation anesthesia with aseptic conditions. Both hind

legs of the rats were disinfected and shaved, operated on by performing a complete tenotomy for the Achilles tendons, and repaired with 5-0 absorbable Prolene sutures using a Kessler stitch technique. For all hind legs, the skin was sutured closed using 5-0 sutures. Weekly, they were examined and weighed to check their correct development. Antibiotic prophylaxis was administered to all specimens before and after surgery. Rats who underwent the surgical procedure were randomly divided into three groups: I) ruptured group: no treatment after the abovementioned surgical procedures, II) Fe-AAO group: subcutaneous injected with Fe-AAO (1 mg/mL, 50 μL) at the Achilles tendon defect site, and III) Co-AAO group: subcutaneous injected with Co-AAO (1 mg/mL, 50 μL) at the Achilles tendon defect site. And rats who didn't conduct the surgical procedure were called the healthy group. Before sacrifice, the rats were conducted for gait analysis and ultrasound examination, and the repaired tendons were harvested at 5 weeks for macroscopic adhesion evaluation, histological hematoxylin and eosin (H&E), Masson, collagen I and collagen III immunofluorescence analysis to assess the recovery.

***In vivo* biocompatibility evaluation**

The hemolysis assay was performed on the basis of previously reported methods with some modifications[1]: The fresh whole blood samples collected with EDTA-coated tubes were centrifuged at 4 °C (1 000 g, 10 min). After the supernatant was removed, the blood samples were diluted 50-fold with saline to obtain 2% red blood cell solution. Then 0.5 mL cells were mixed with the as-fabricated nanoparticles (0.5 mL) diluted in saline to different concentrations (62.5, 125, 250, 500, 1000 μg/mL). 0.5 mL of cells were mixed with 0.5 mL deionized water or 0.5 mL saline as the positive control or negative control, respectively. Each group was duplicated in three parallel experiments. After incubation for 3 h at 37 °C, the mixtures were centrifuged (1,000 g, 10 min), and the supernatant absorbance was measured at 540 nm via a microplate reader. The hemolysis ratio was calculated as explained in our previous report through the following formula:

$$P = (A_S - A_N)/(A_P - A_N) \times 100\%$$

Where A_S is the absorbance resulting from the mixture of biocatalysts and red blood cells, and A_N and A_P represent the absorbance of negative and positive controls, respectively.

For serum blood biochemistry tests, the blood from the aorta abdominalis of rats was collected and used for assessing two important indicators of hepatic function as aspartate aminotransferase (AST) and alanine aminotransferase (ALT) and two indicators of kidney function as blood urea nitrogen (BUN) and creatinine (CRE) at 5 weeks postoperatively. Briefly, the samples were centrifuged at 15 000 × g for 15 min after sitting for 2 h at 4 °C, then the serum was carefully separated and placed in anticoagulant tubes for future tests on the chemistry analyzer. Besides, the rats were sacrificed to harvest major organs (including heart, liver, spleen, lung, and kidney) for H&E staining and histological analysis.

Statistical analysis

All data are expressed in this manuscript as mean ± SD. All the results have been performed at least three times by independent experiments. The one-way ANOVA analysis is used to analyze the statistical significance among more than 2 groups. The statistical analysis is performed using GraphPad Prism 8.0 (GraphPad Software Inc.). Asterisks indicate significant differences (*P<0.05, **P<0.01, ***P<0.001, ****P<0.0001, ns: no significant differences).

Supplementary Figures

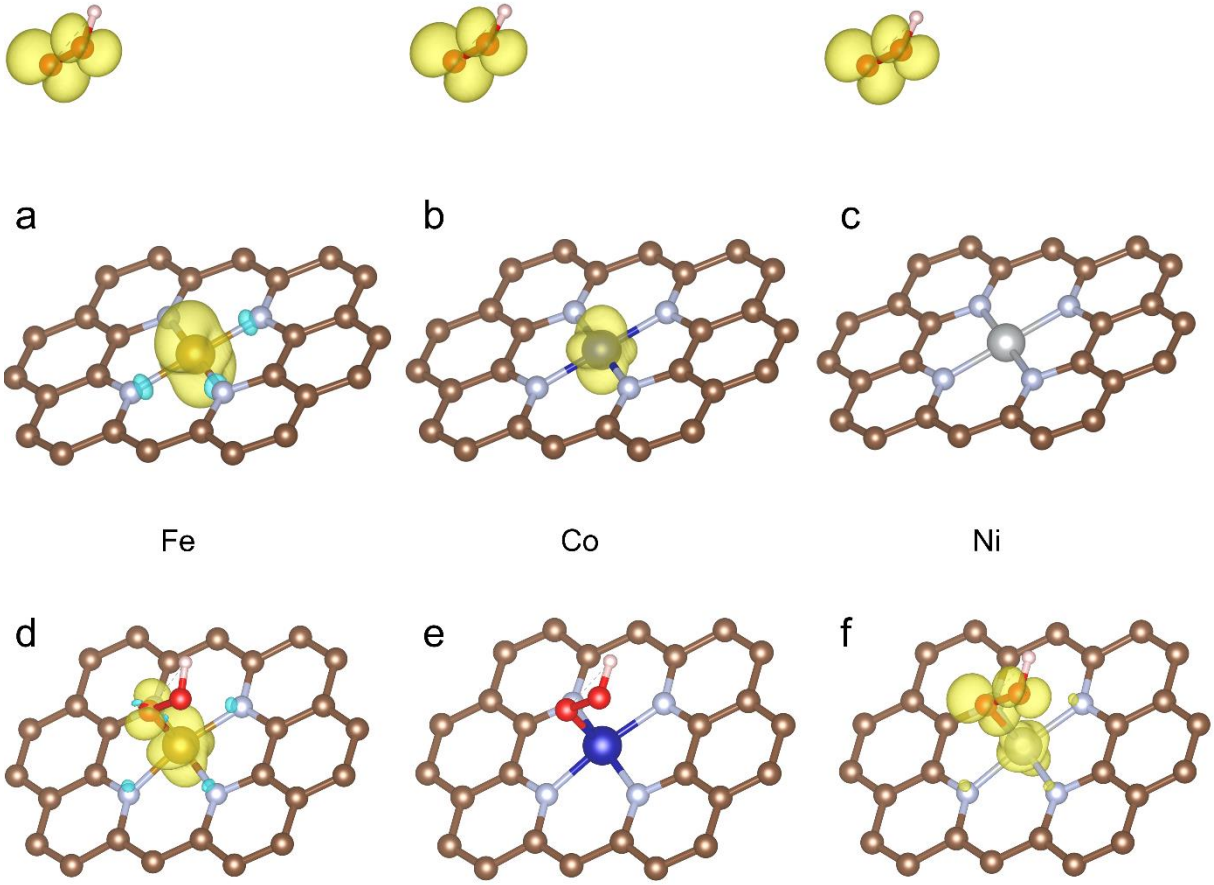

Figure S1. The calculated spin charge density of (a-c) before and (d-f) after the interaction of FA-N_4 with *OOH (the cutoff of the density-difference isosurface is 0.005 e/Bohr^3; Fe: golden, Co: blue, Ni: silver, C: brown, N: grey, O: red, H: white).

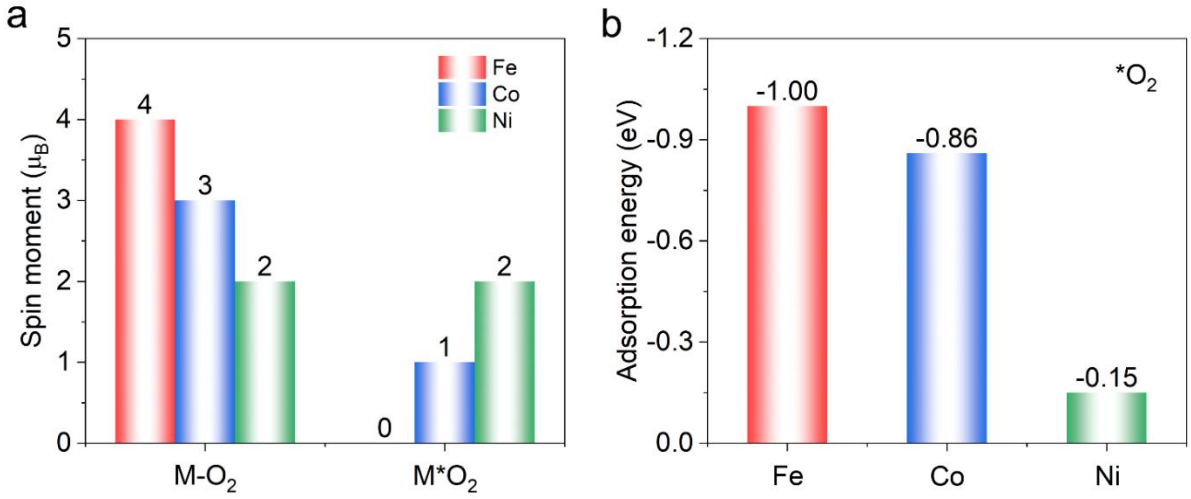

Figure S2. (a) The calculated magnetic moment statistics of the system before (M-O_2) and after (M*O_2) the interaction of FA-N_4 with *O_2. (b) The binding energy of *O_2 with FA-N_4.

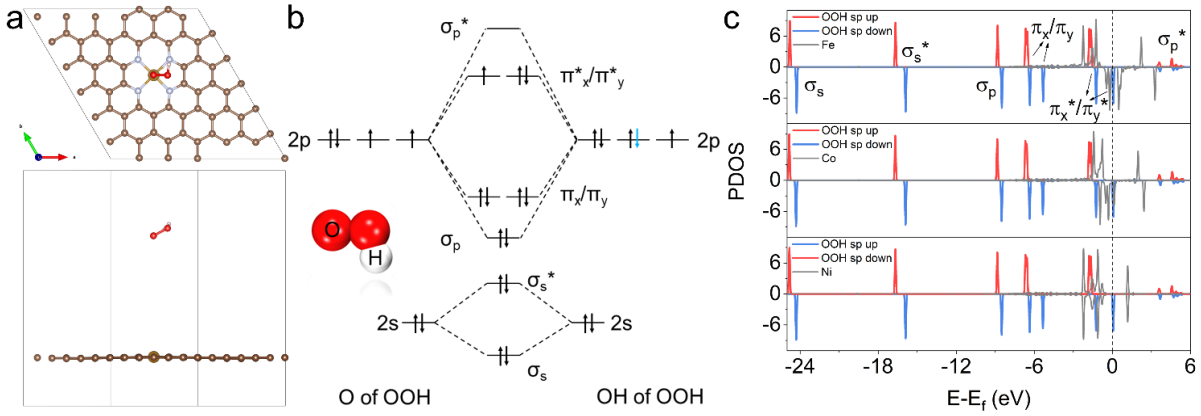

Figure S3. (a) The optimized model before the interaction of FA-N_4 and *OOH. (b) The molecular orbital diagram of *OOH. (c) The calculated PDOS of FA-N_4-OOH (before interaction), where the *OOH molecular orbitals arrangement corresponds to (a).

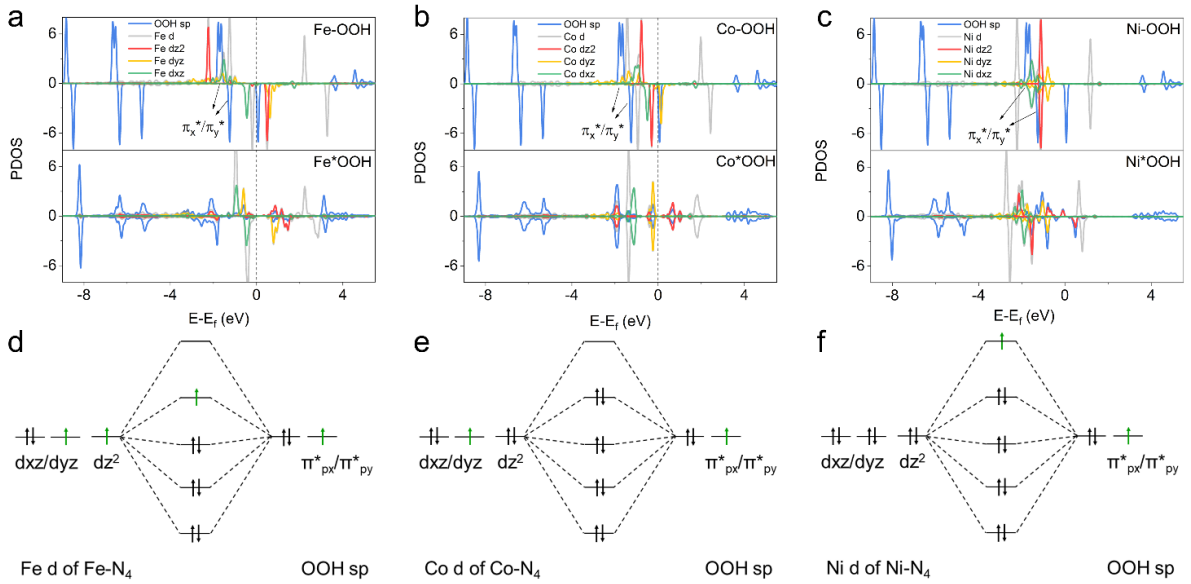

Figure S4. The calculated PDOS of before (M-OOH) and after (M*OOH) the interaction of OOH with (a) Fe-N_4, (b) Co-N_4, and (c) Ni-N_4. The molecular orbital diagrams of (d) Fe-N_4*OOH, (e) Co-N_4*OOH, and (f) Ni-N_4*OOH.

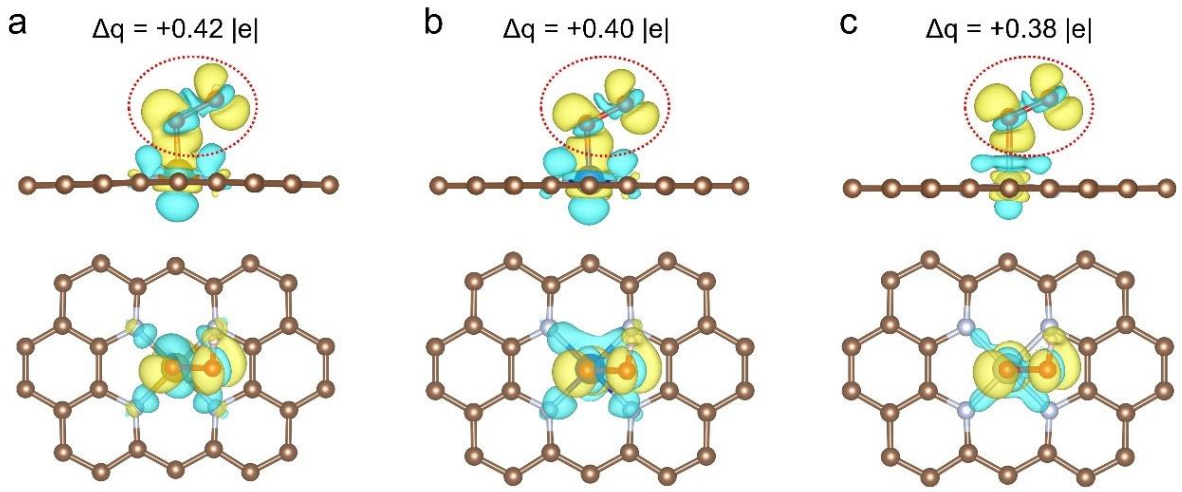

Figure S5. The charge density differences and Bader analysis of OOH with (a) Fe-N_4, (b) Co-N_4 and (c) Ni-N_4 (cyan and yellow represent charge depletion and accumulation, respectively, the cutoff of the density-difference isosurface is 0.002 e/Bohr^3).

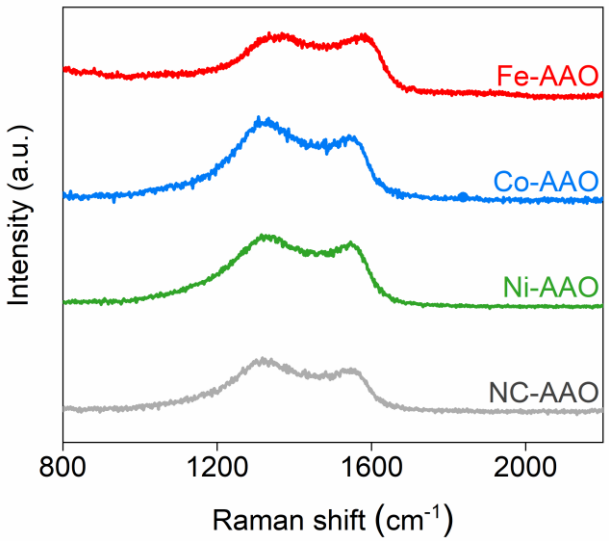

Figure S6. Raman spectra of different FA-AAOs and NC-AAO biocatalysts.

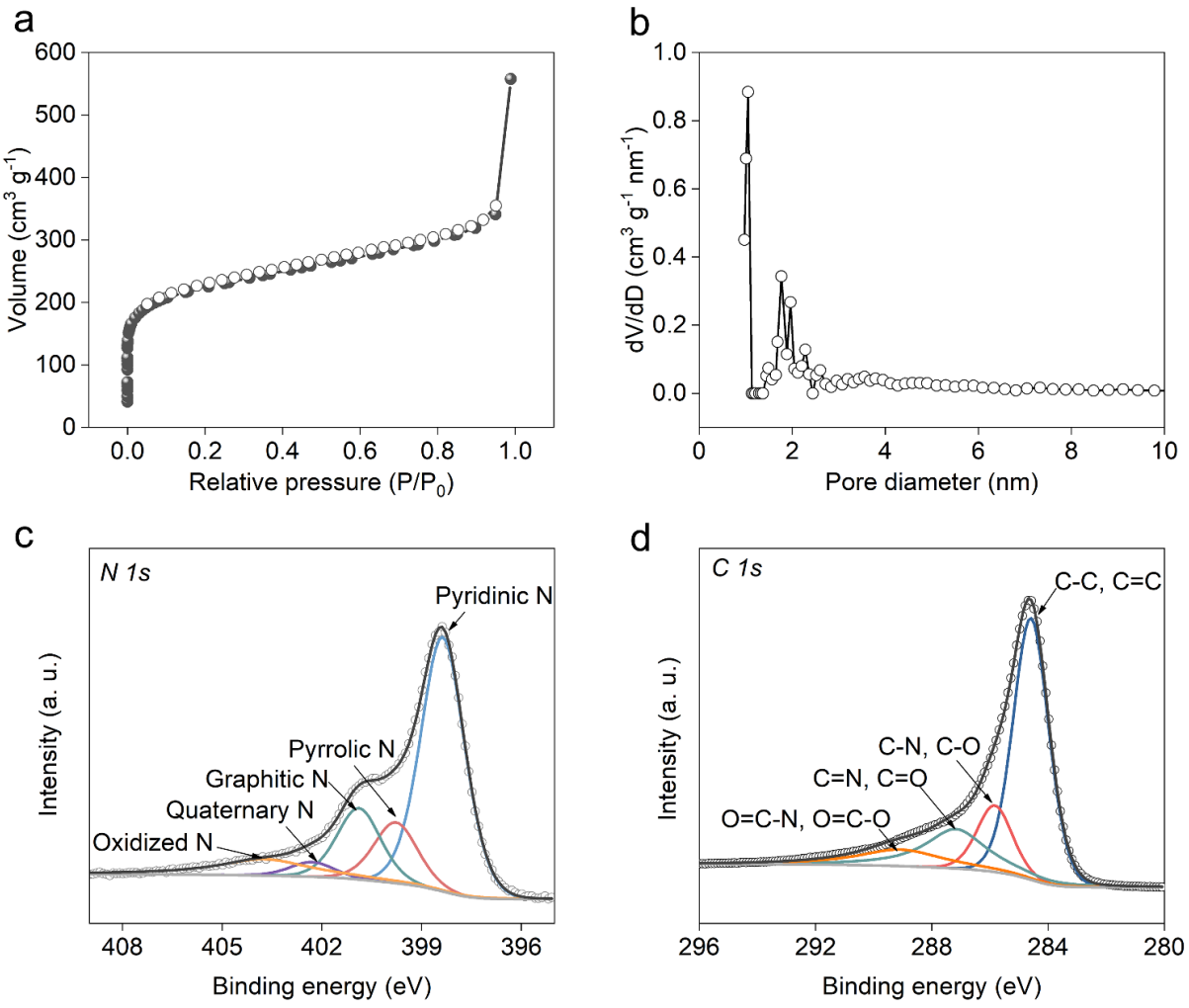

Figure S7. (a) N_2 isothermal adsorption-desorption curves and (b) pore distribution of NC-AAO. High-resolution (c) N 1s spectra and (d) C 1s spectra of NC-AAO. The bare nanocubic carbon without hetero-metal ion is also synthesized, which indicates the doping of atomic hetero-metal will not change the morphology of metal-organic precursors.

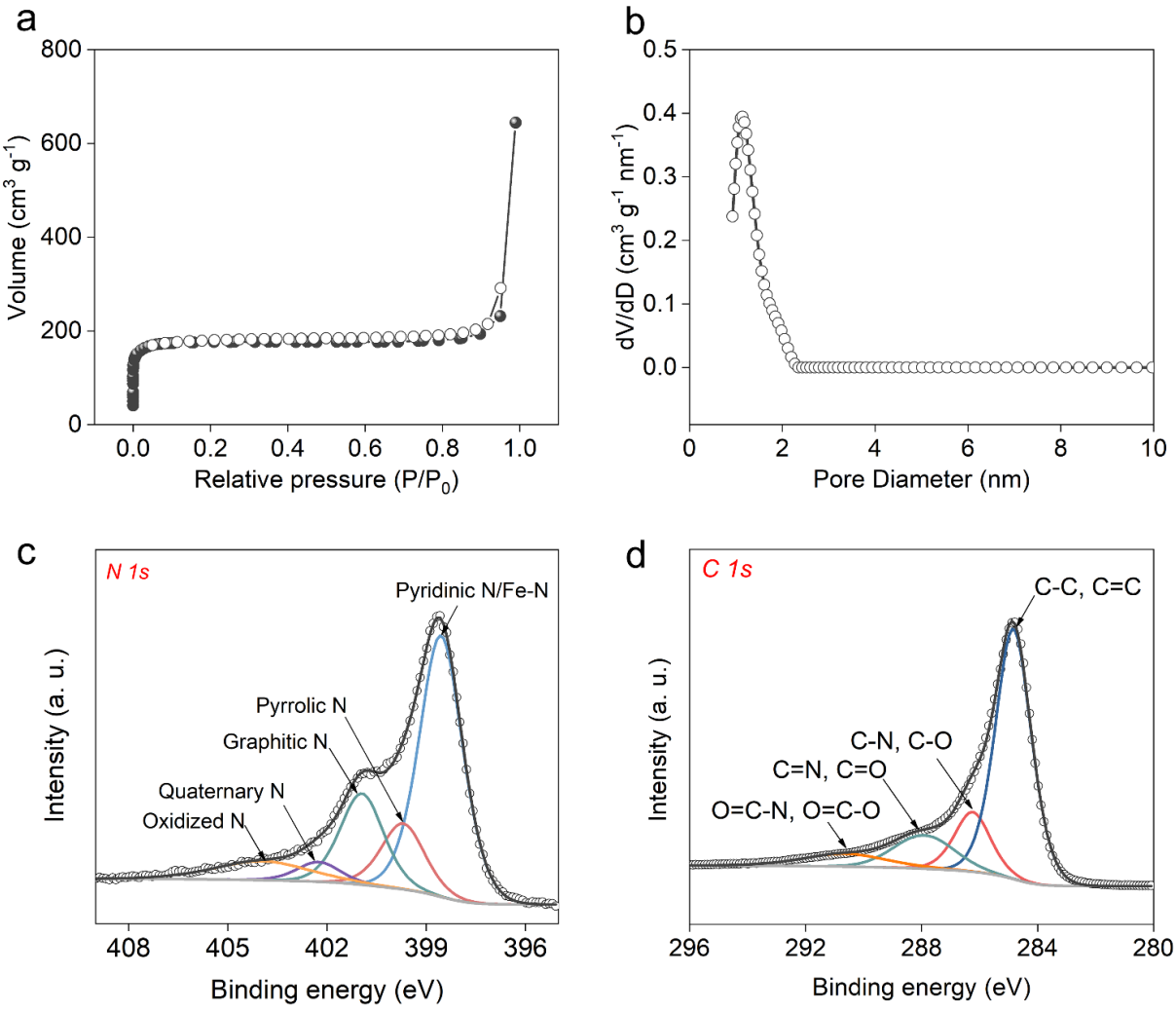

Figure S8. (a) N_2 isothermal adsorption-desorption curves and (b) pore distribution of Fe-AAO. High-resolution (c) N 1s spectra and (d) C 1s spectra of Fe-AAO.

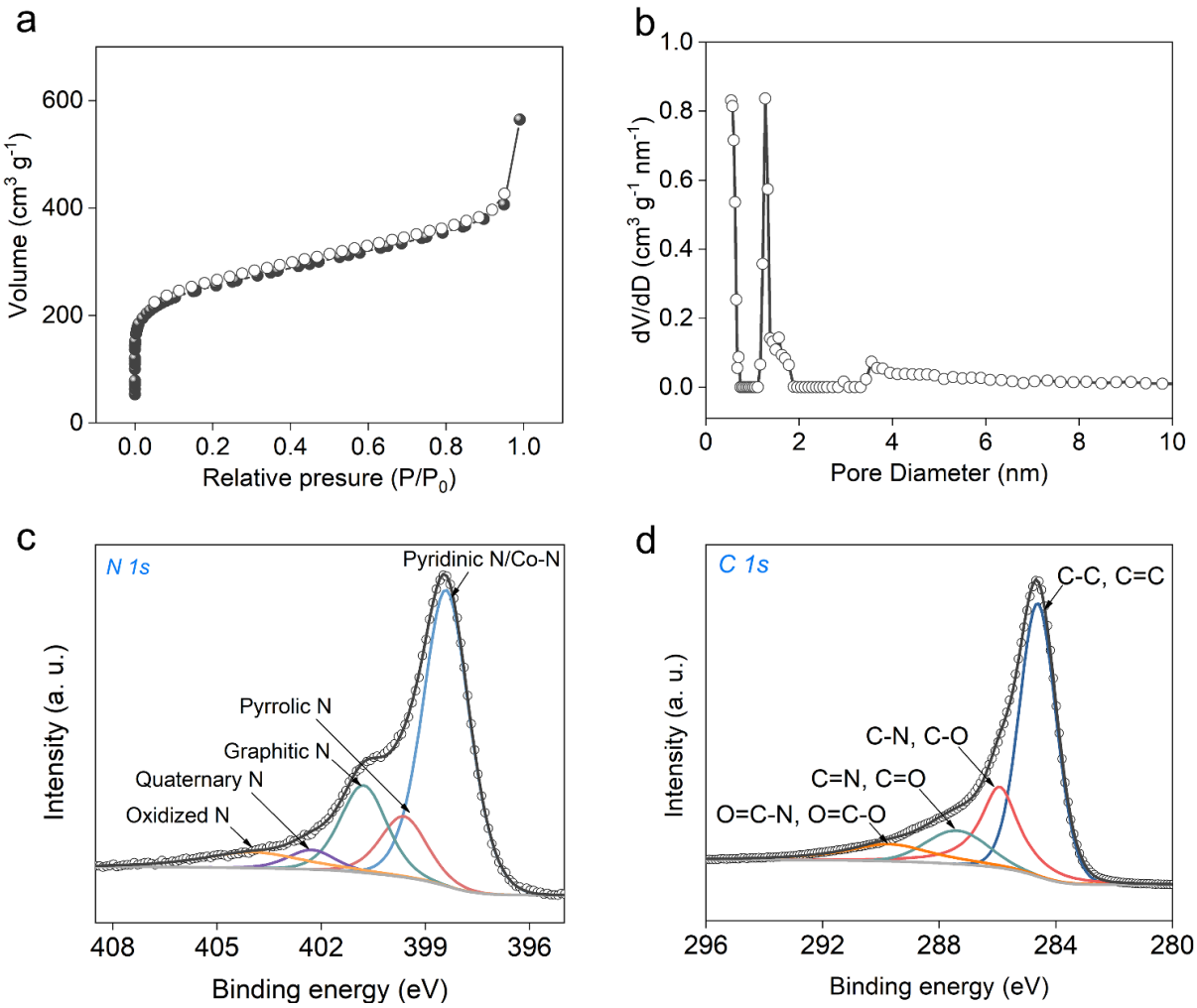

Figure S9. (a) N_2 isothermal adsorption-desorption curves and (b) pore distribution of Co-AAO. High-resolution (c) N 1s spectra and (d) C 1s spectra of Co-AAO.

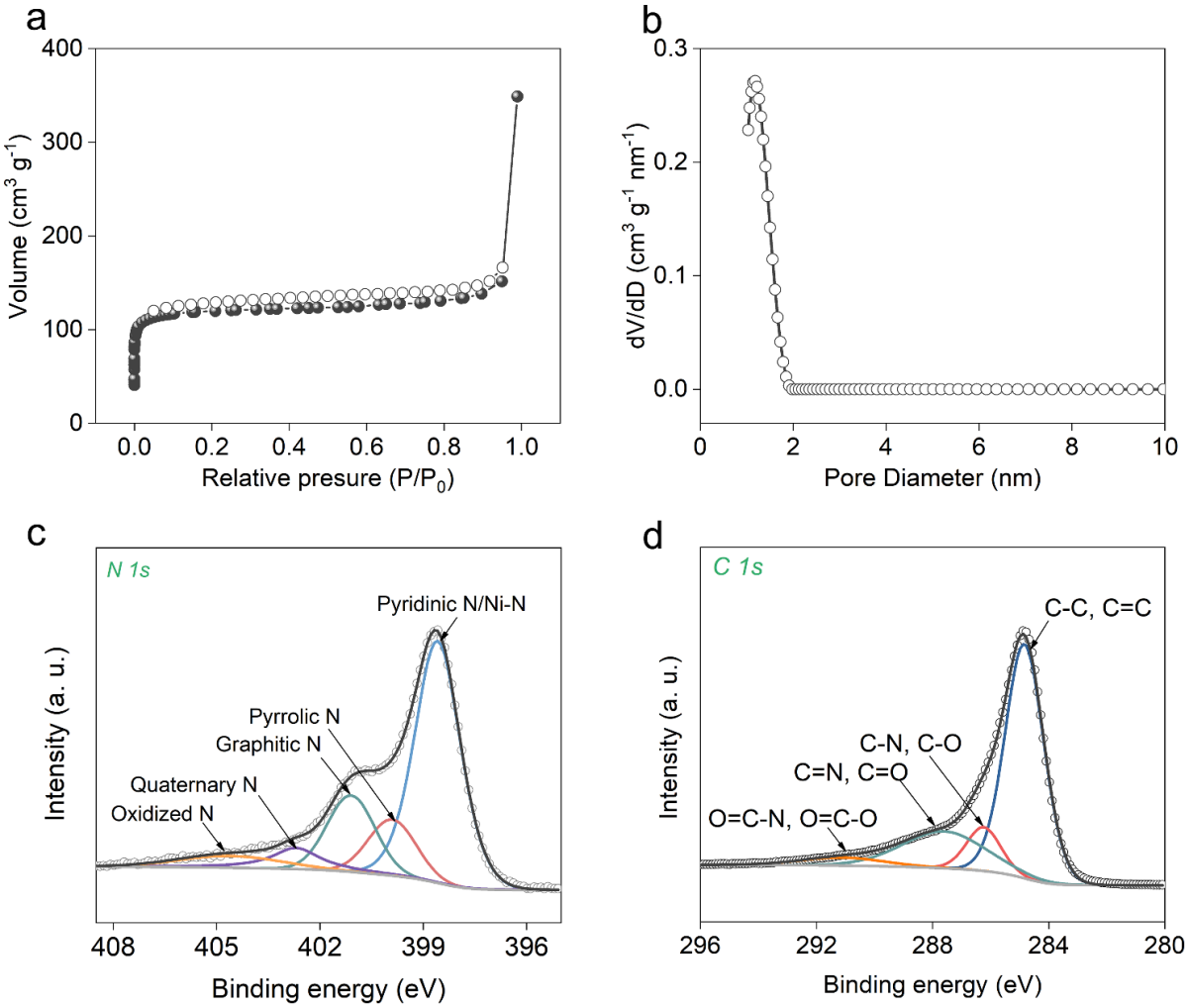

Figure S10. (a) N_2 isothermal adsorption-desorption curves and (b) pore distribution of Ni-AAO. High-resolution (c) N 1s spectra and (d) C 1s spectra of Ni-AAO.

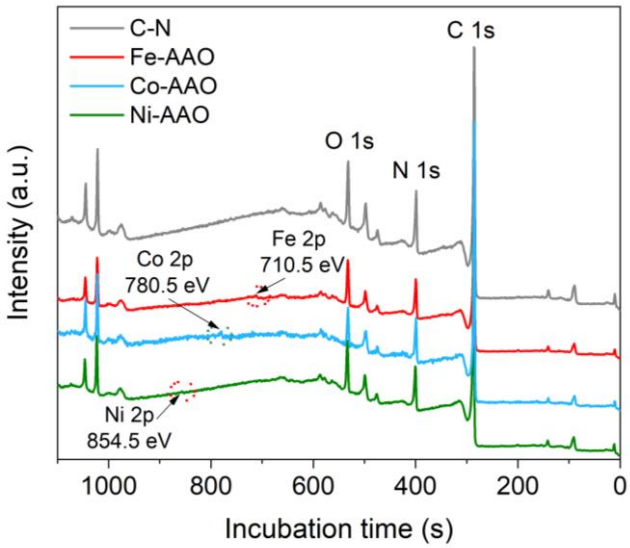

Figure S11. XPS spectra of C-N, Fe-AAO, Co-AAO, and Ni-AAO.

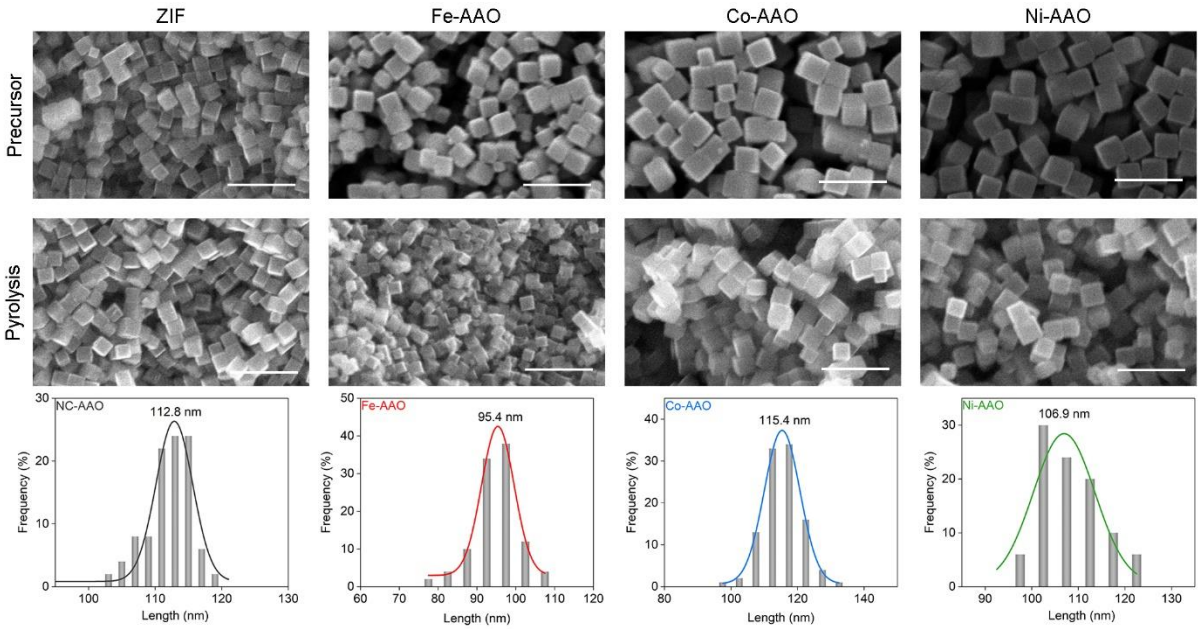

Figure S12. SEM images of different materials before and after calcination, and size distribution histograms of FA-AAOs. Scale bar is 500 nm.

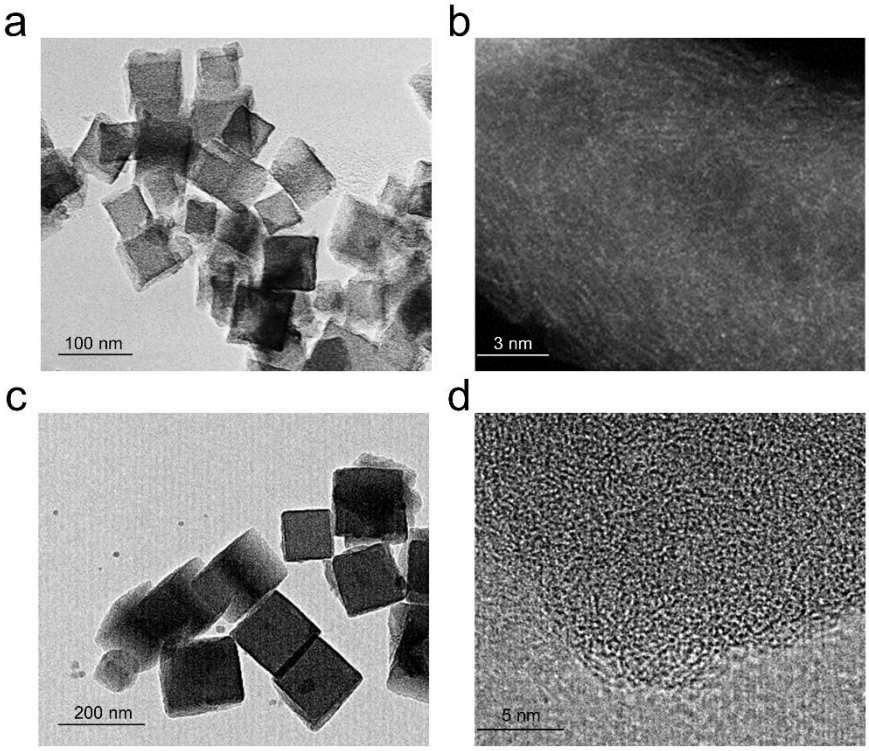

Figure S13. Bright-field STEM images of (a, b) Fe-AAO and (c, d) Co-AAO.

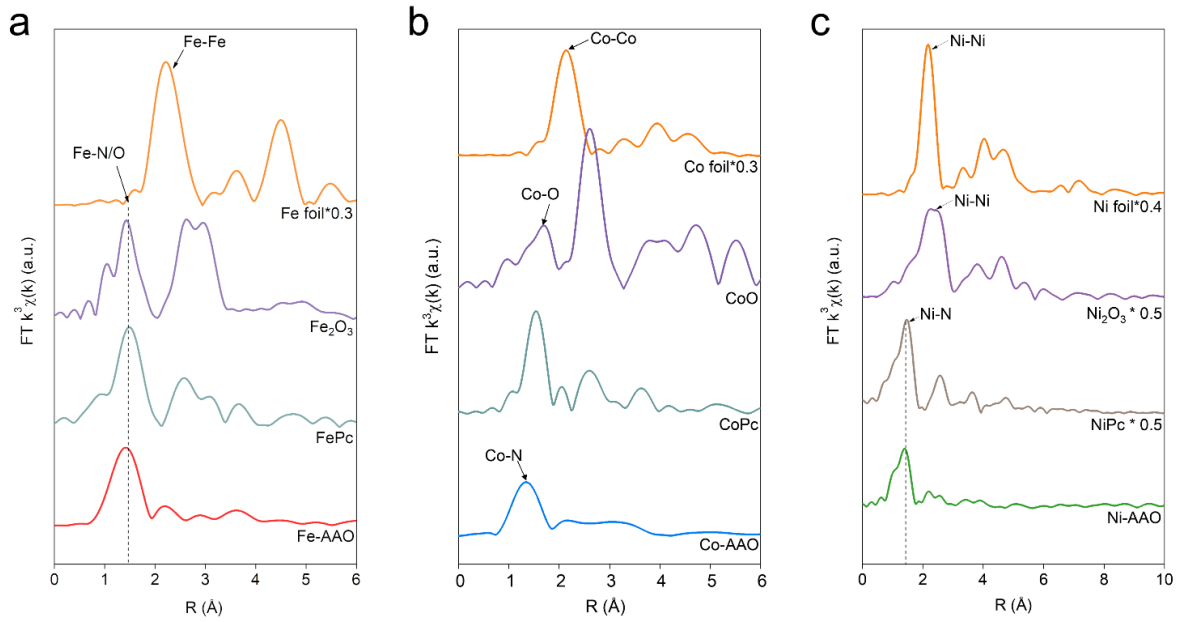

Figure S14. Fourier transform of (a) Fe, (b) Co, and (c) Ni *K*-edge EXAFS of samples.

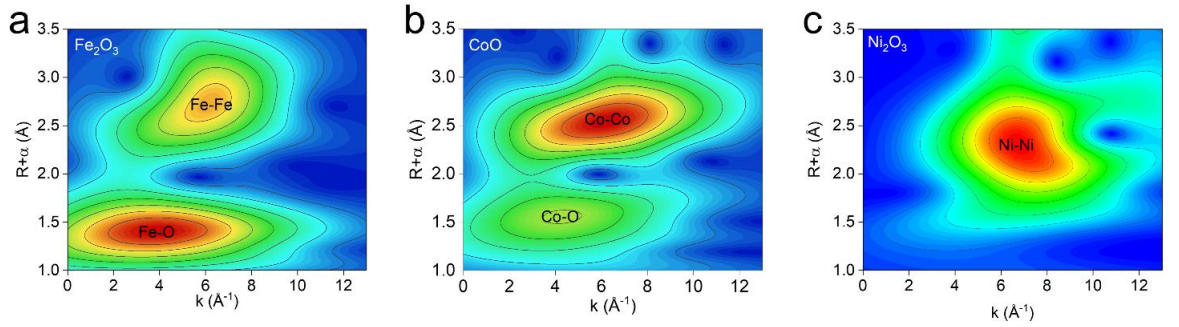

Figure S15. Wavelet transform images at the (a) Fe *K*-edge of Fe_2O_3, (b) Co *K*-edge of CoO, and (c) Ni *K*-edge of Ni_2O_3.

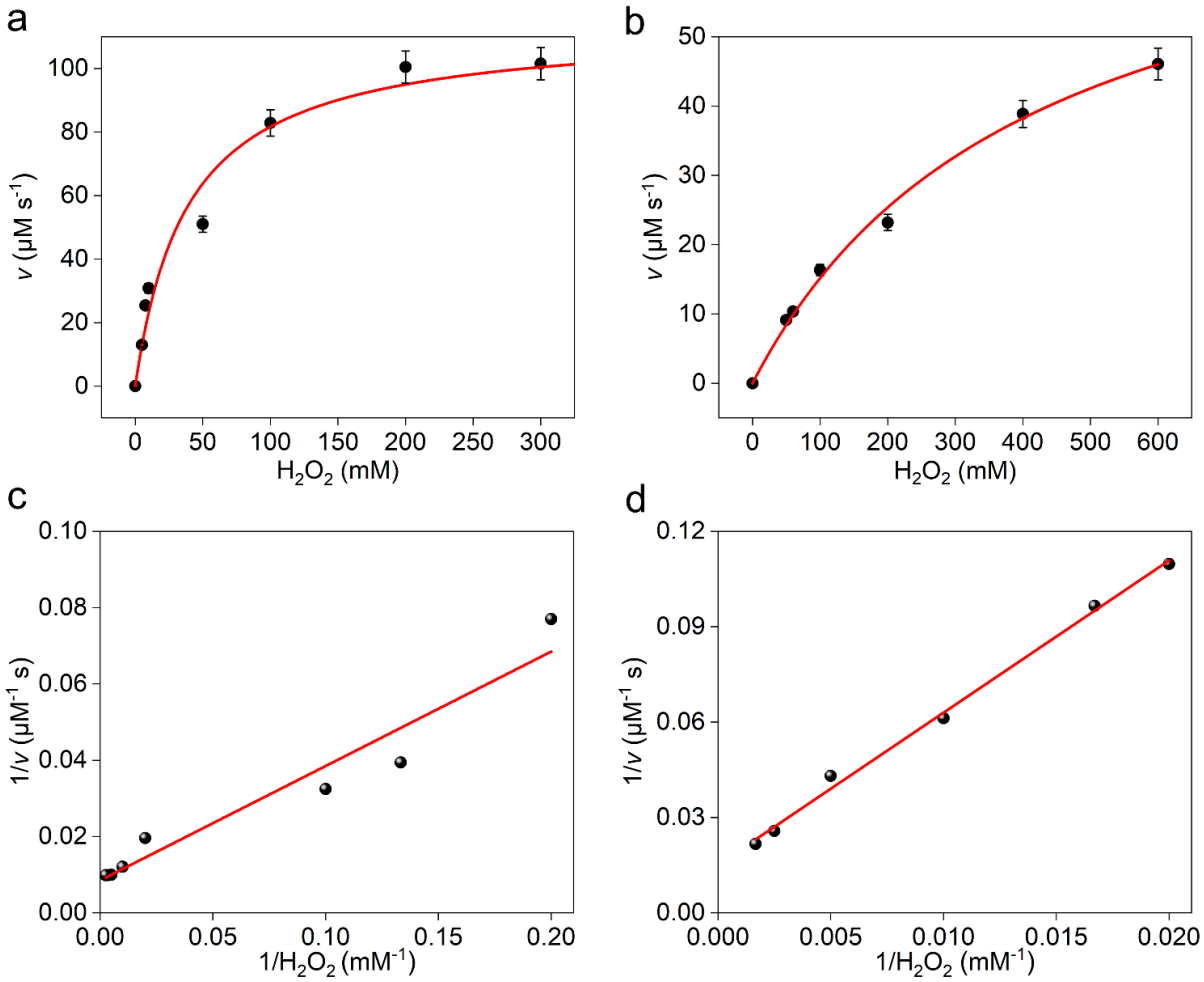

Figure S16. Steady-state constant of CAT-like activity for (a) Fe-AAO and (b) Co-AAO with H_2O_2 as substrate. The corresponding double reciprocal plots of (c) Fe-AAO and (d) Co-AAO.

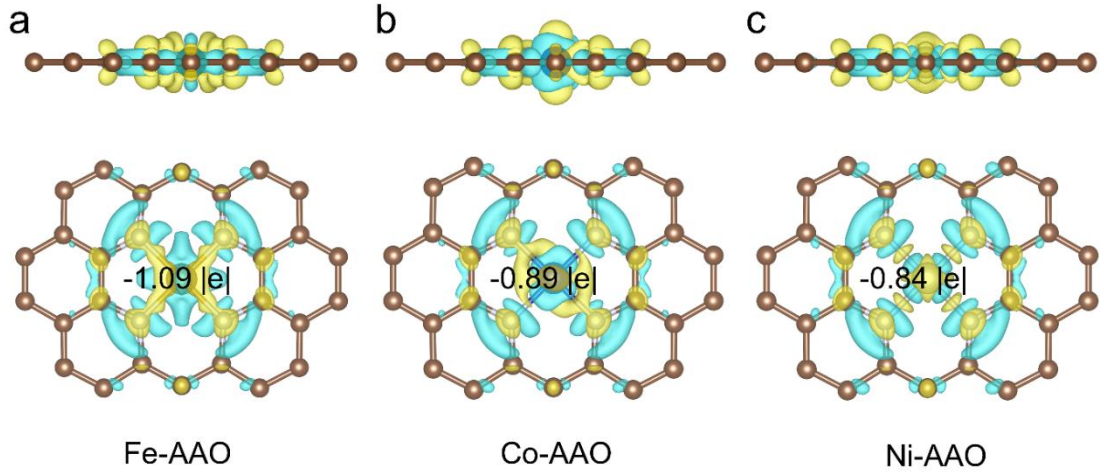

Figure S17. The charge density differences and Bader analysis of FA-AAOs (cyan and yellow represent charge depletion and accumulation, respectively, the cutoff of the density-difference isosurface is 0.005 e/Bohr^3).

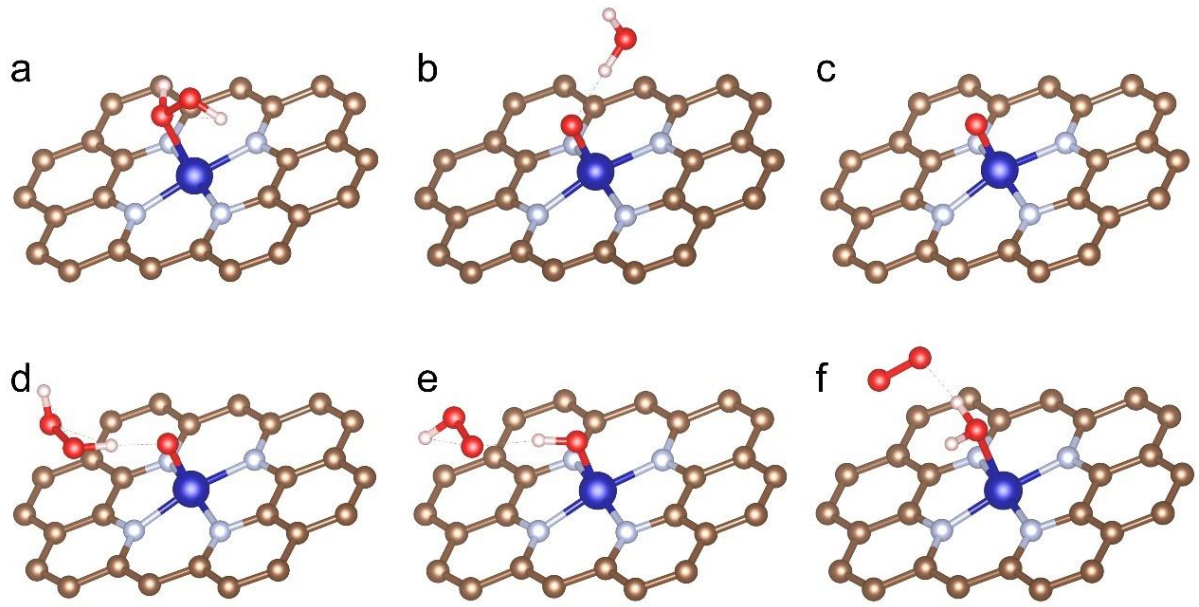

Figure S18. The optimized adsorption conformations of different reaction intermediates on Co-AAO. a) H_2O_2, b) O-H_2O, c) O, d) O-H_2O_2, e) OH-OOH, and f) H_2O-O_2 (Co: blue, N: grey, C: brown, O: red, H: white).

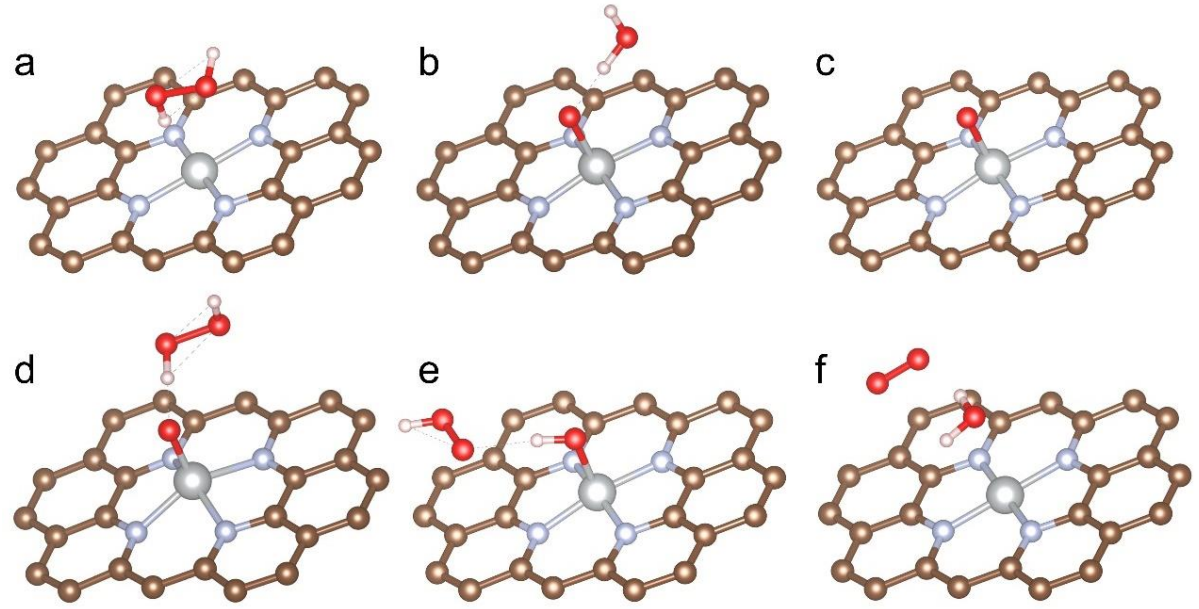

Figure S19. The optimized adsorption conformations of different reaction intermediates on Ni-AAO. a) H_2O_2, b) O-H_2O, c) O, d) O-H_2O_2, e) OH-OOH, and f) H_2O-O_2 (Ni: silver, N: grey, C: brown, O: red, H: white).

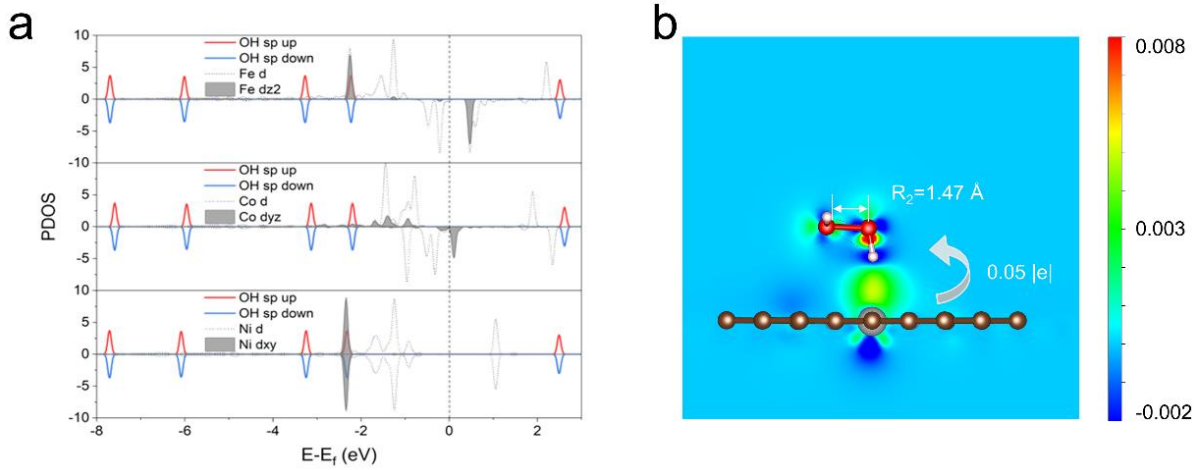

Figure S20. (a) The calculated PDOS before the interaction of FA-AAOs with H_2O_2. b) The charge density differences of Ni-AAO*H_2O_2.

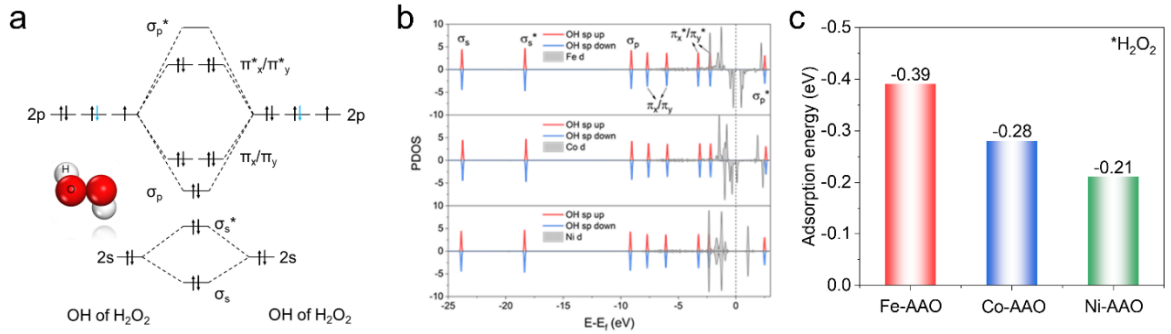

Figure S21. a) The molecular orbital diagram of the H_2O_2 molecule. b) The calculated PDOS of FA-AAO-H_2O_2 (before interaction), where the H_2O_2 molecular orbitals arrangement corresponds to a). c) The binding energy of H_2O_2 with FA-AAOs.

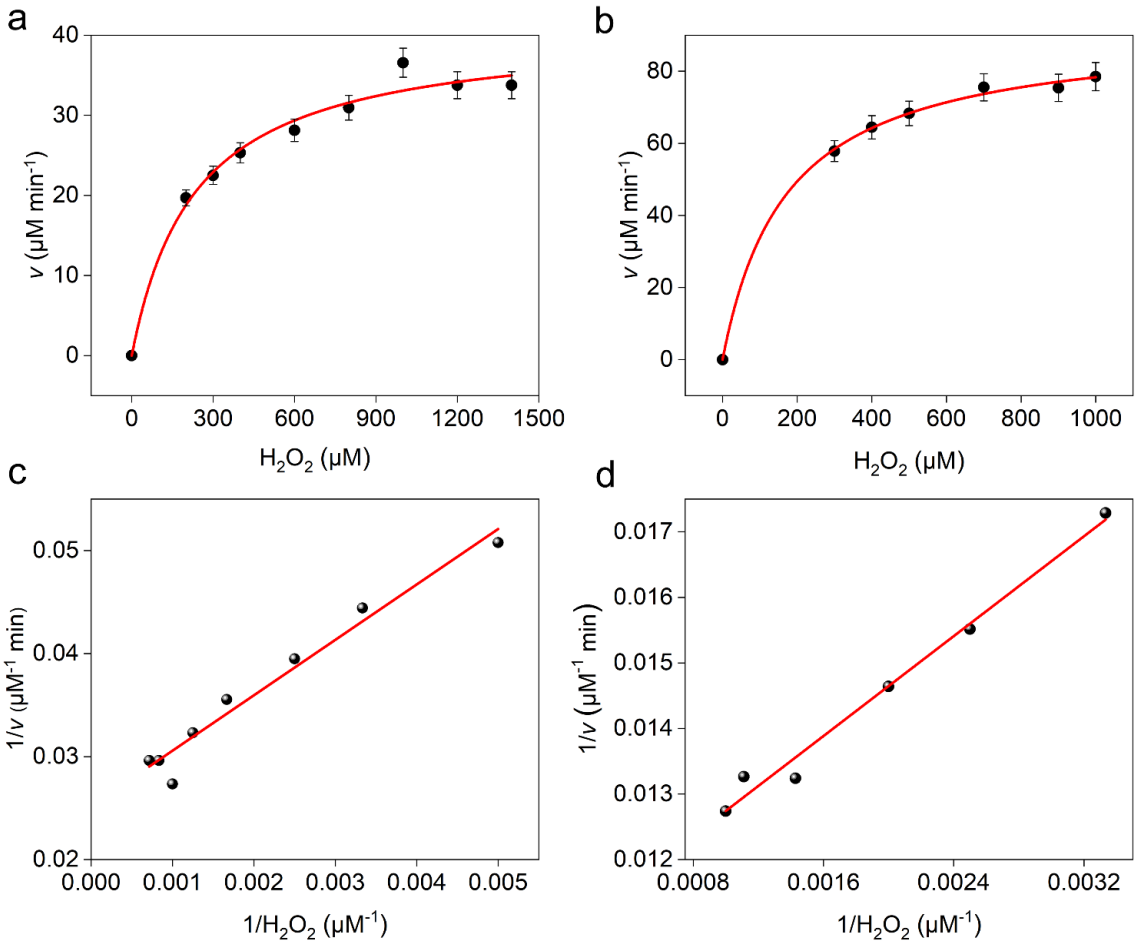

Figure S22. Steady-state constant of GPx-like activity for (a) Fe-AAO and (b) Co-AAO with H_2O_2 as substrate. The corresponding double reciprocal plots of (c) Fe-AAO and (d) Co-AAO.

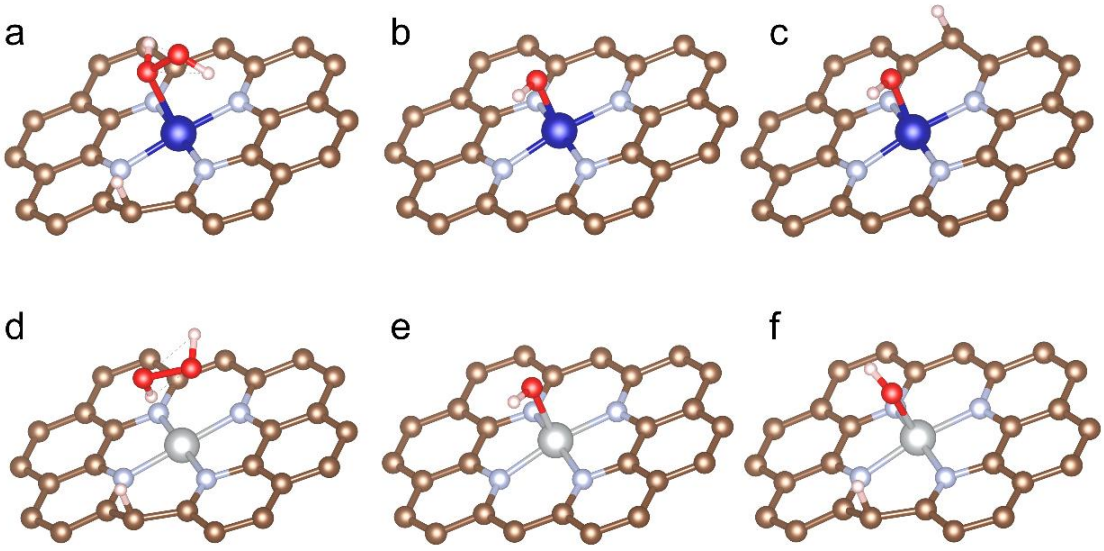

Figure S23. The optimized adsorption conformations of different reaction intermediates on Co-N_4 and Ni-N_4. a) H_2O_2_H, b) OH, and c) OH_H (Co: blue, Ni: silver, N: grey, C: brown, O: red, H: white).

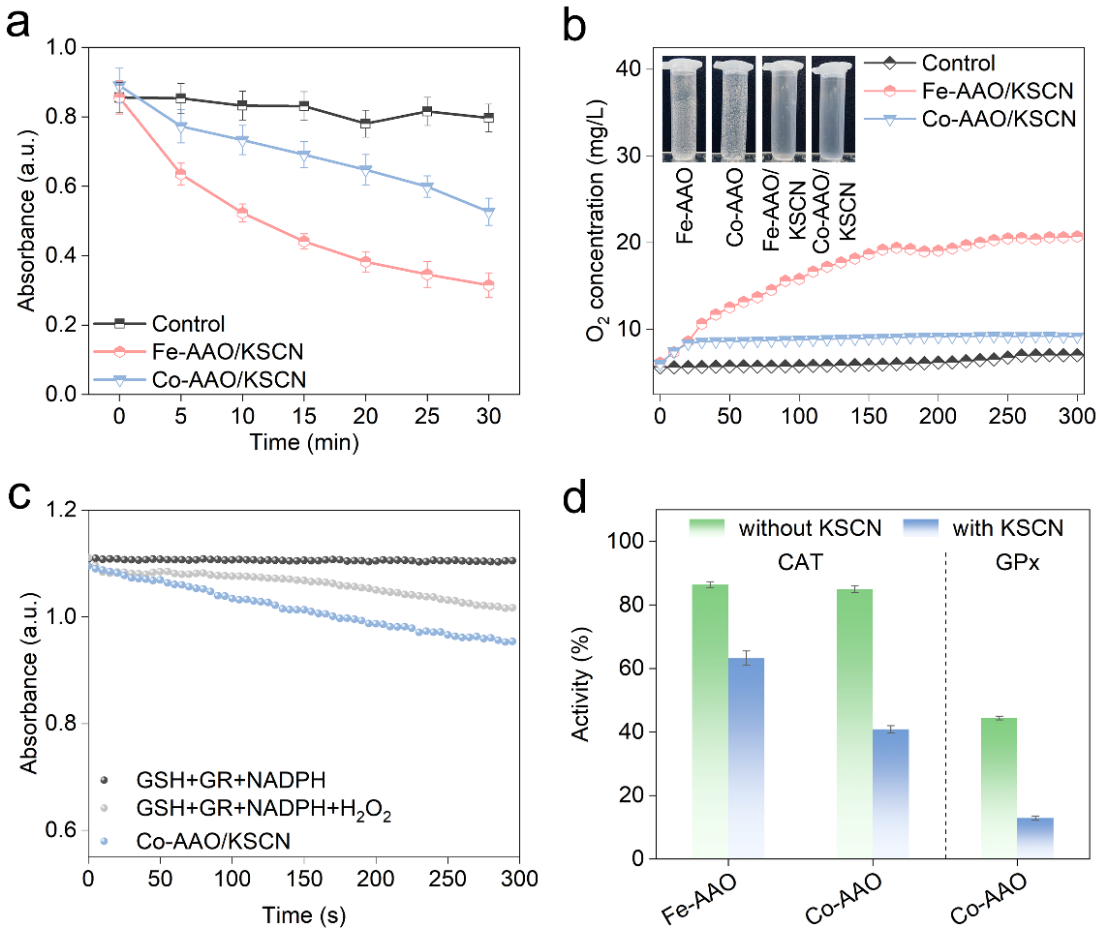

Figure S24. (a) The dynamic H_2O_2 scavenging activities, and (b) the dynamic O_2 generation property of FA-AAOs with KSCN. Inset is the image of the O_2 generation property. (c) The UV-vis absorption spectra of GPx activities. (d) Active site poison tests of biocatalysts via KSCN.

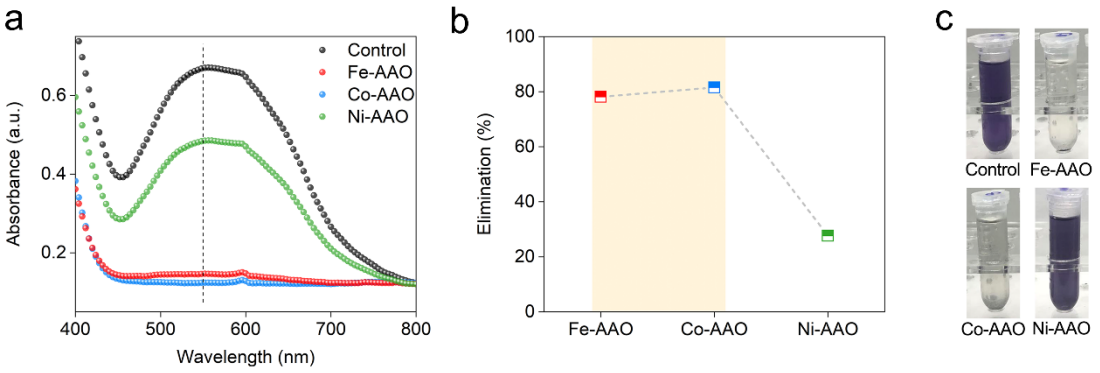

Figure S25. (a) UV-vis absorption spectra of superoxide dismutase-like activity. (b) The clearance rate of $\bullet O_2^-$ for FA-AAOs. (c) The image of the $\bullet O_2^-$ scavenging property.

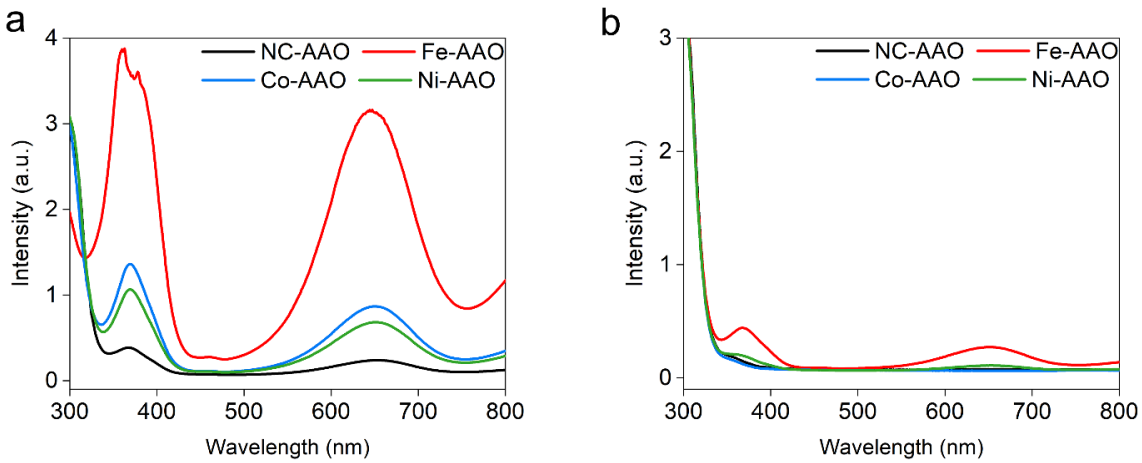

Figure S26. The peroxidase-like activity of AAOs in (a) pH 4.5 and (b) pH 7.4 condition.

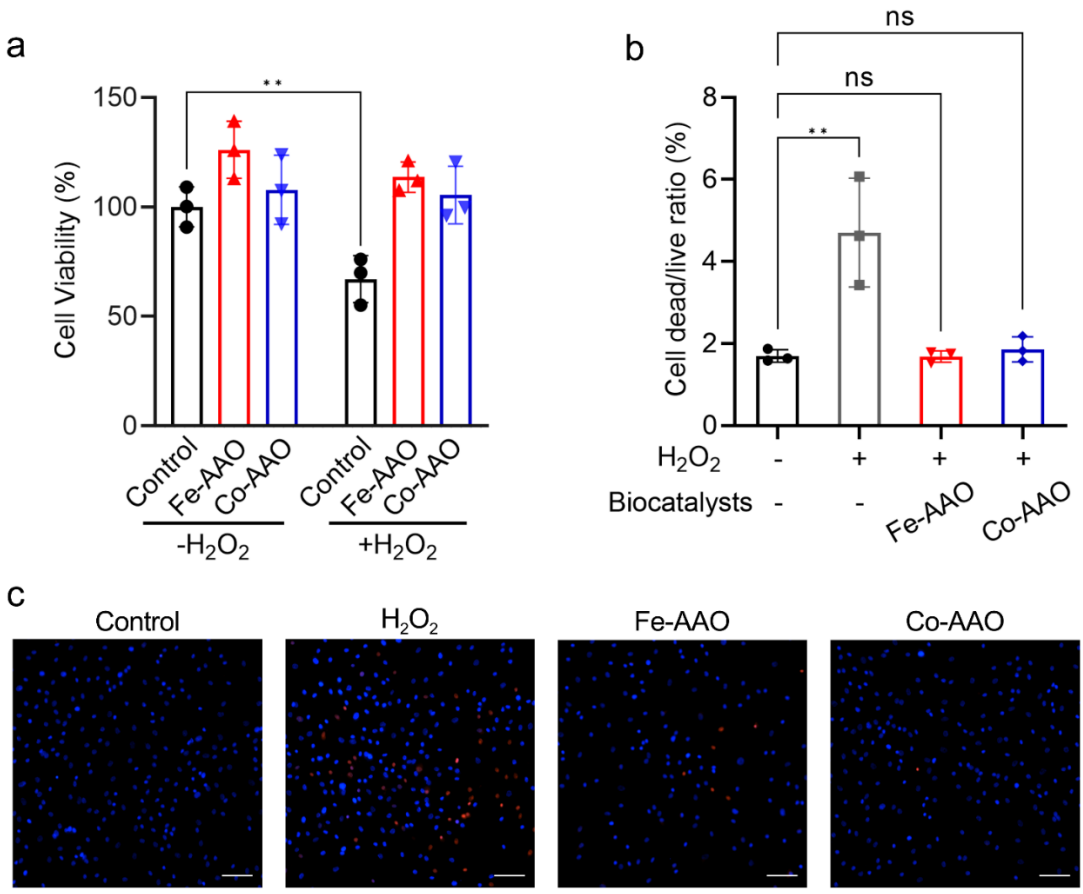

Figure S27. (a) In vitro cytotoxicity with different treatments towards hMSCs after incubation for 24 h (n = 3). (b) Dead/live cell ratio and (c) the fluorescence staining of dead/live cells (red represents dead cell, blue represents cell nucleus) with ROS and FA-AAOs (n = 3). Scale bar is 100 μm. Data are presented as mean ± SD. *$P < 0.05$, **$P < 0.01$, ns represents no significant differences.

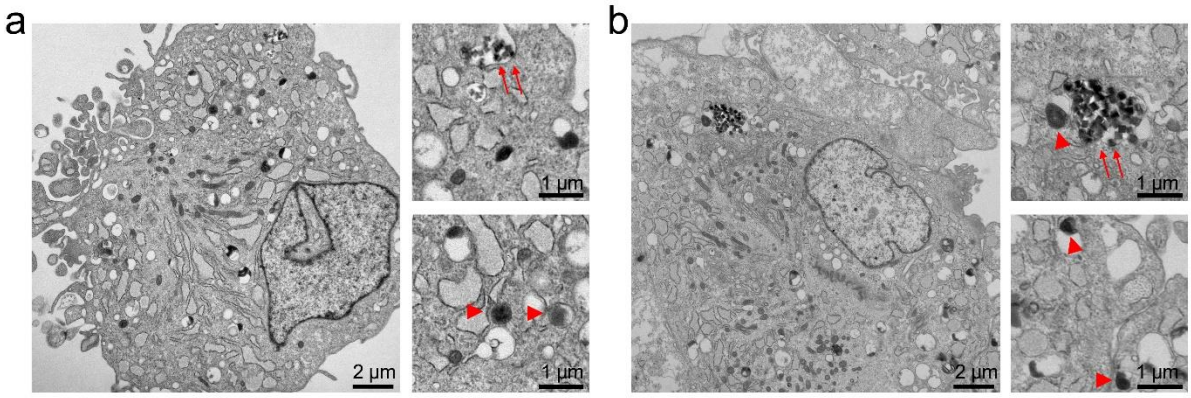

Figure S28. TEM images to observe the uptake of (a) Fe-AAO and (b) Co-AAO in hMSCs (red arrows: AAOs in phagosomes; red triangle: lysosome).

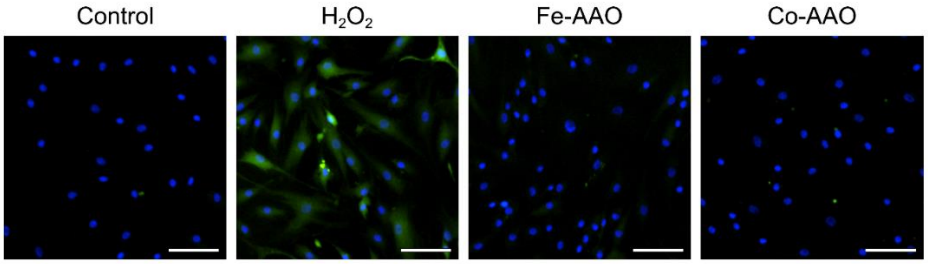

Figure S29. Representative ROS staining images (green: ROS, blue: DAPI) of hMSCs under different treatment conditions. Scale bar is 100 μm.

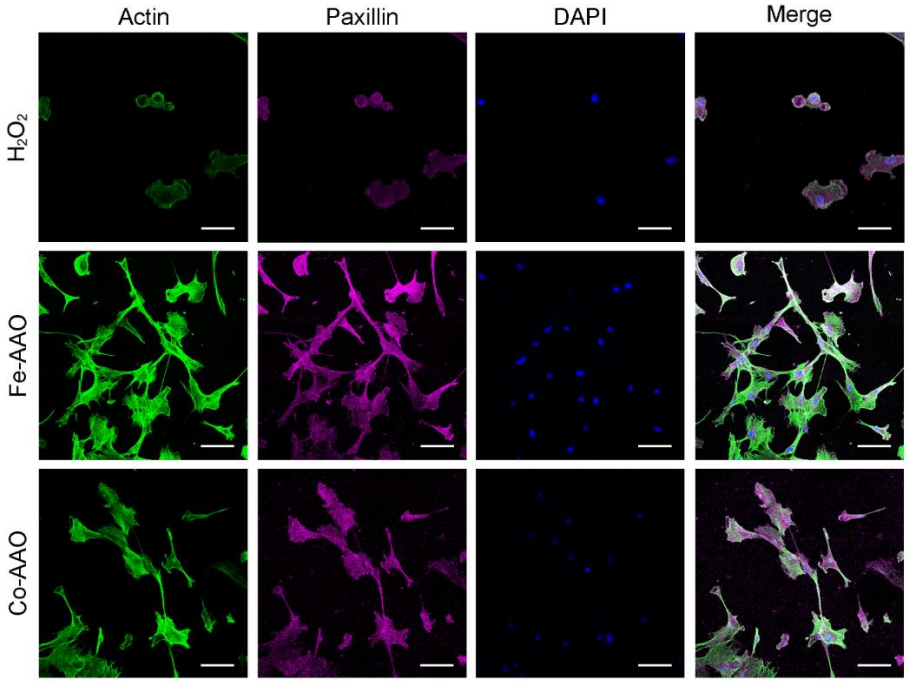

Figure S30. Representative nucleus, F-actin, and Paxillin immunofluorescence staining images of hMSCs with different treatments. Scale bar is 100 μm.

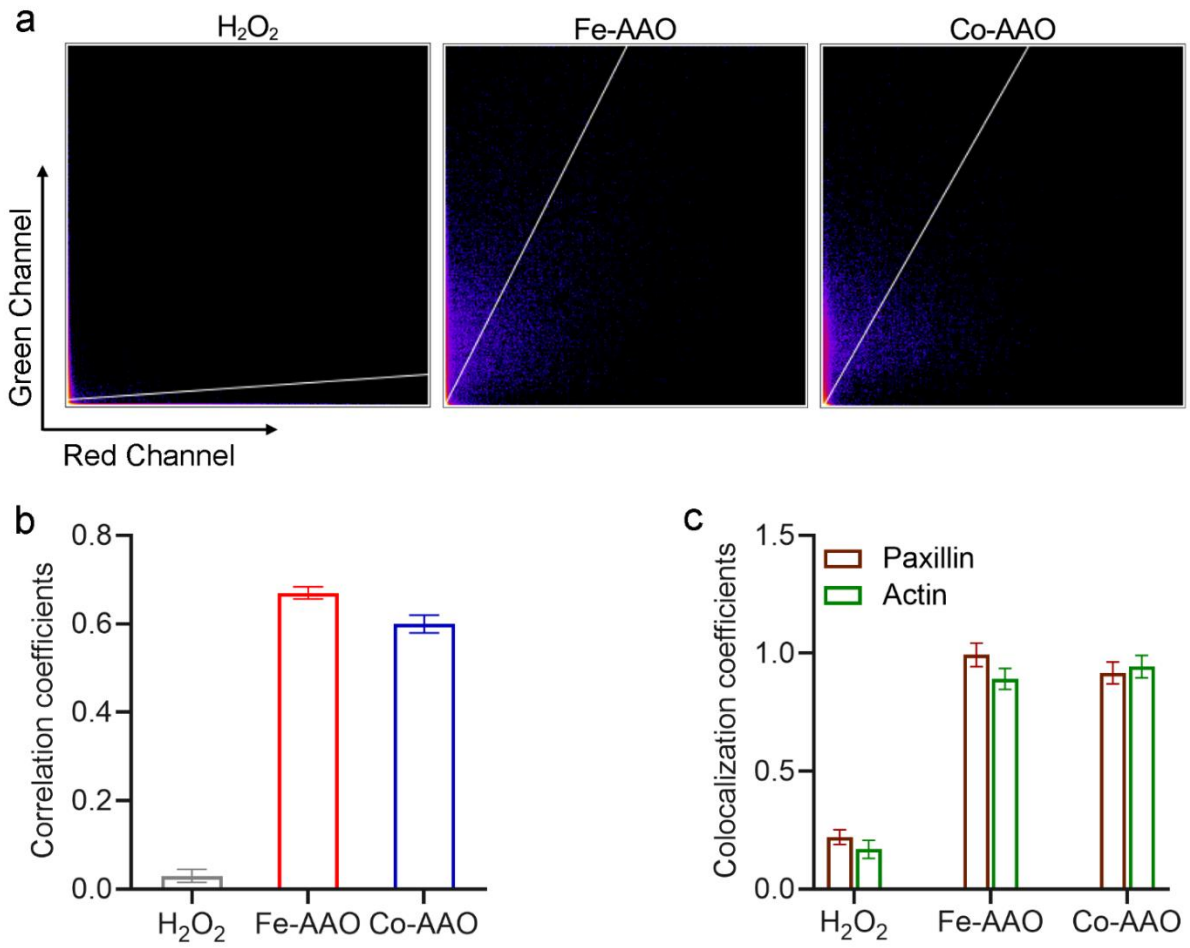

Figure S31. (a) Colocalization images of Paxillin (red) and Actin (green) in the CLSM results, and corresponding quantitative analysis of (b) correlation coefficients and (c) colocalization coefficients. Through quantitative colocalization analysis of CLSM, the correlation and colocalization coefficients between the green channel (Actin) and red channel (Paxillin) in the FA-AAO groups are higher than that in the H_2O_2 group, which indicates that the probability of co-occurrence of red fluorescence (focal adhesions) and green fluorescence (cytoskeleton) is greater in the FA-AAO groups.

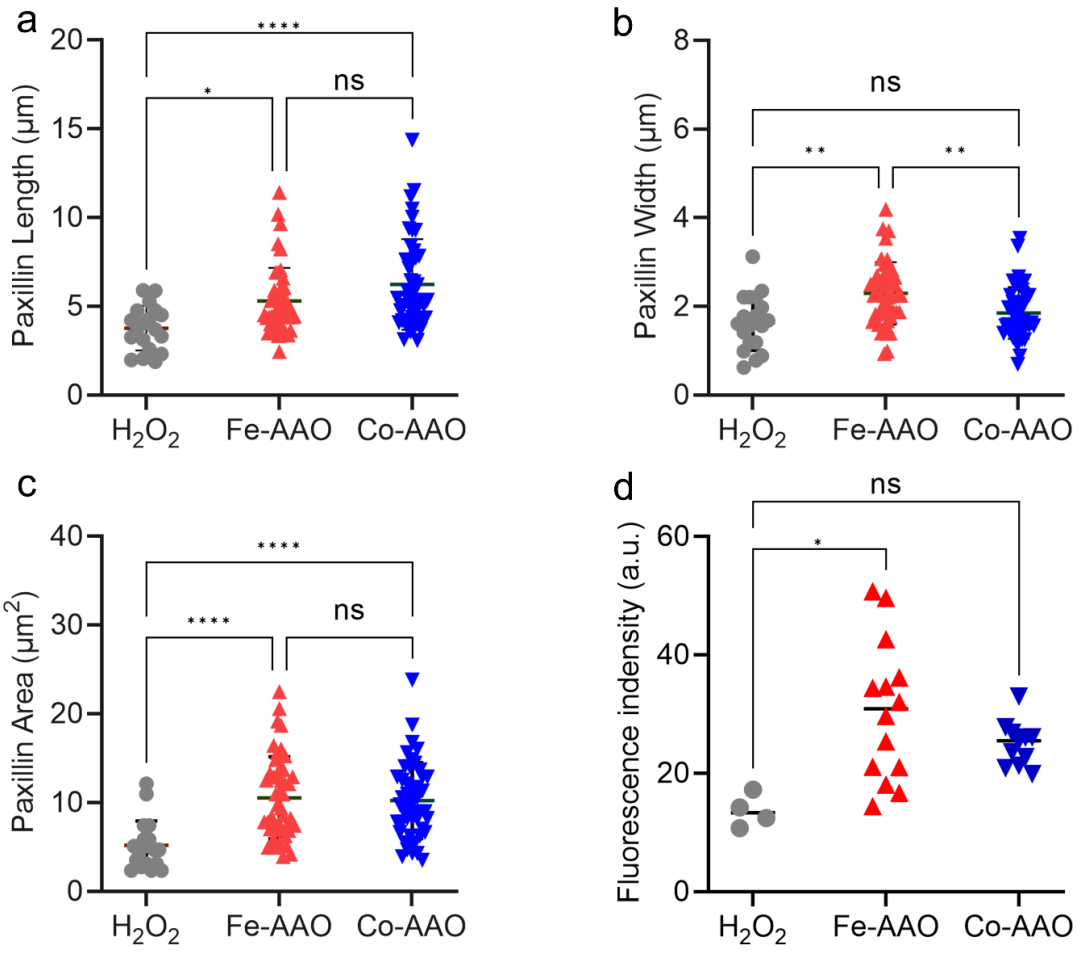

Figure S32. The semi-quantitative analysis of (a) length, (b) width, (c) area, and (d) fluorescence intensity of paxillin distributions. *$P < 0.05$, **$P < 0.01$, ***$P < 0.001$, ****$P < 0.0001$, ns represents no significant differences.

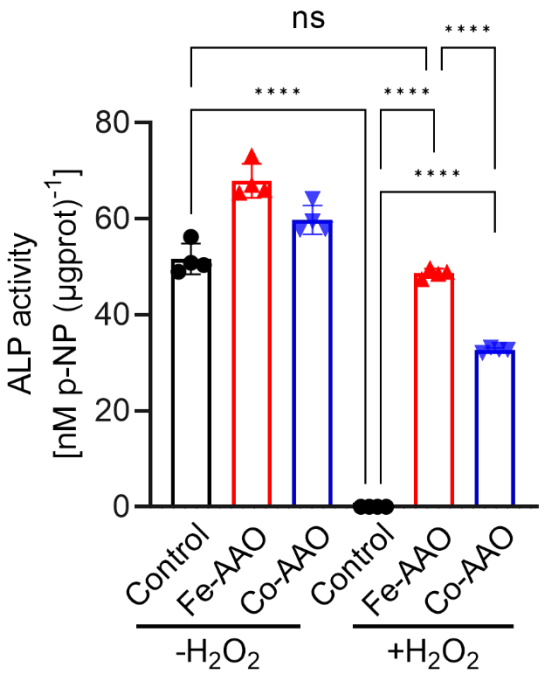

Figure S33. Quantitative assay of ALP activity with different conditions (n = 4). Data are presented as mean ± SD. *$P < 0.05$, **$P < 0.01$, ***$P < 0.001$, ****$P < 0.0001$, ns represents no significant differences.

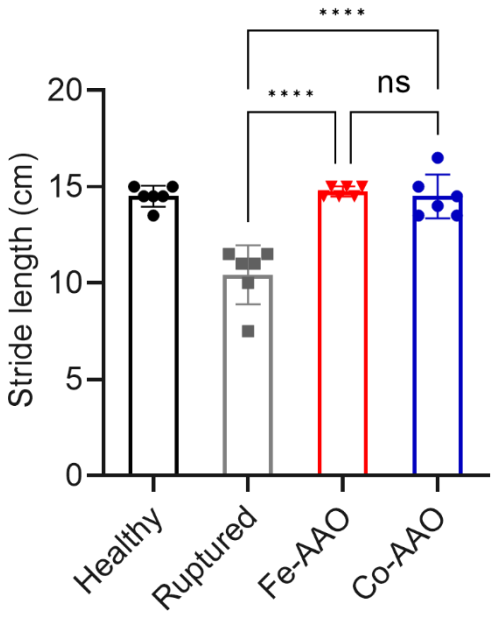

Figure S34. The stride length from different groups at postinjury (n = 6). Data are presented as mean ± SD. *$P < 0.05$, **$P < 0.01$, ***$P < 0.001$, ****$P < 0.0001$, ns represents no significant differences.

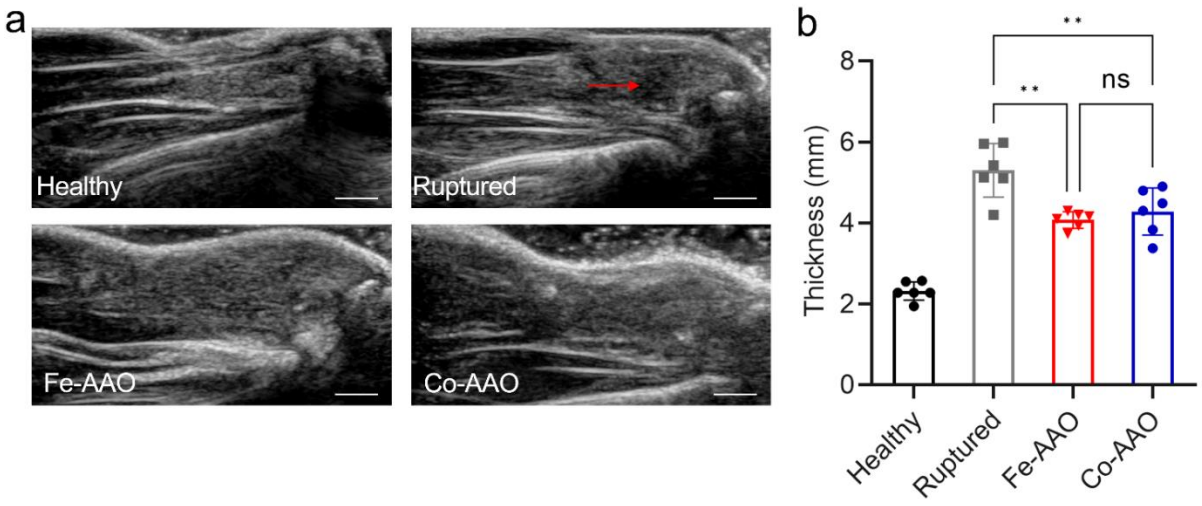

Figure S35. (a) Ultrasound examination (long axis, red arrow represents heterogeneous echo) and (b) corresponding thickness of rats' Achilles tendon (n = 6). *P < 0.05, **P < 0.01, ns represents no significant differences. Scale bar is 2.5 mm.

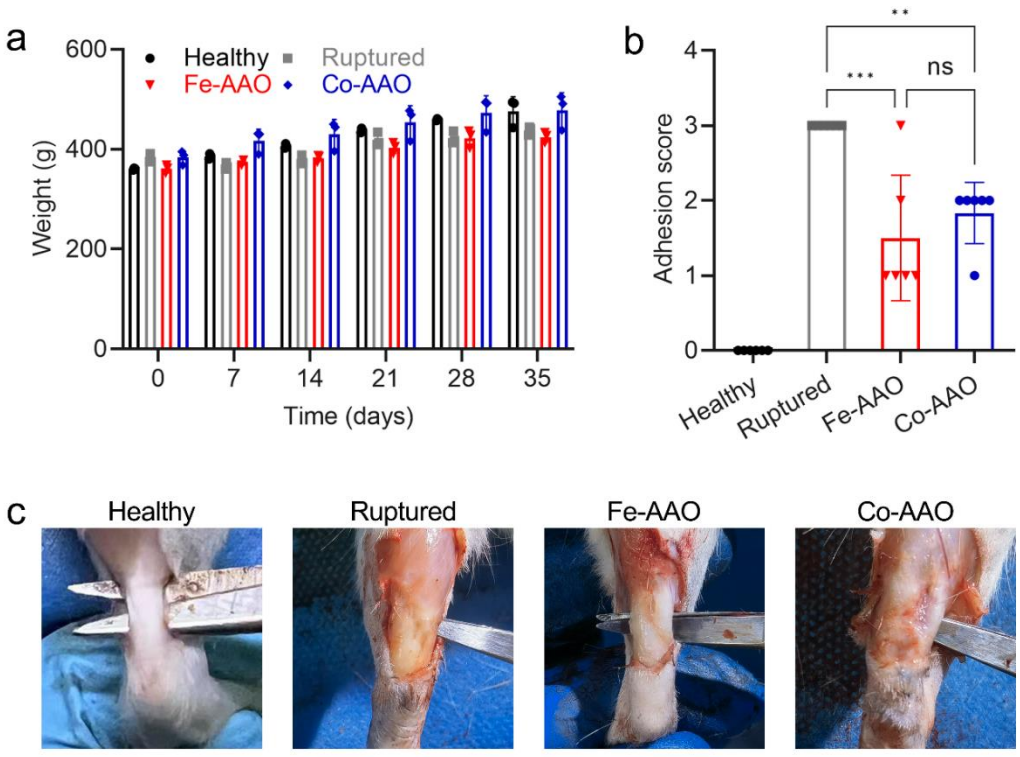

Figure S36. (a) The weight changes from different groups during treatments (n = 3). (b) The adhesion score at the macroscopic level (n = 6). (c) Representative images of tendon appearance at 5 weeks postoperatively. Data are presented as mean ± SD. *P < 0.05, **P < 0.01, ***P < 0.001, ns represents no significant differences.

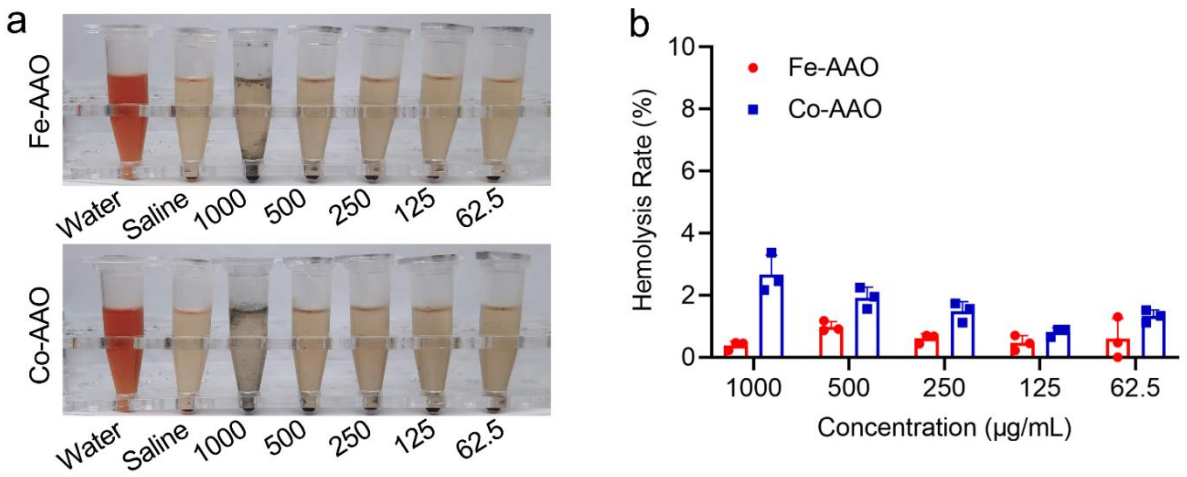

Figure S37. (a) In vitro hemolysis test of FA-AAOs and (b) corresponding hemolysis rate (n = 3). Data are presented as mean ± SD.

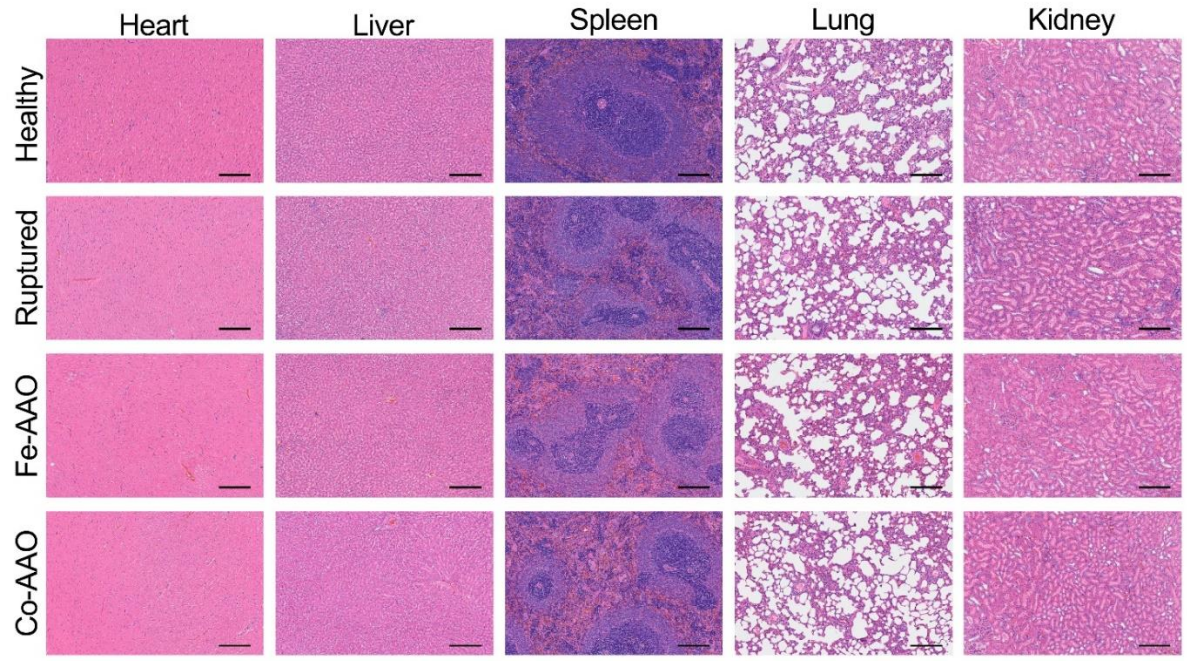

Figure S38. In vivo toxicity evaluation of FA-AAOs to major organs (heart, liver, spleen, lung, and kidney) at 5 weeks after subcutaneous administration. Scale bar is 250 μm.

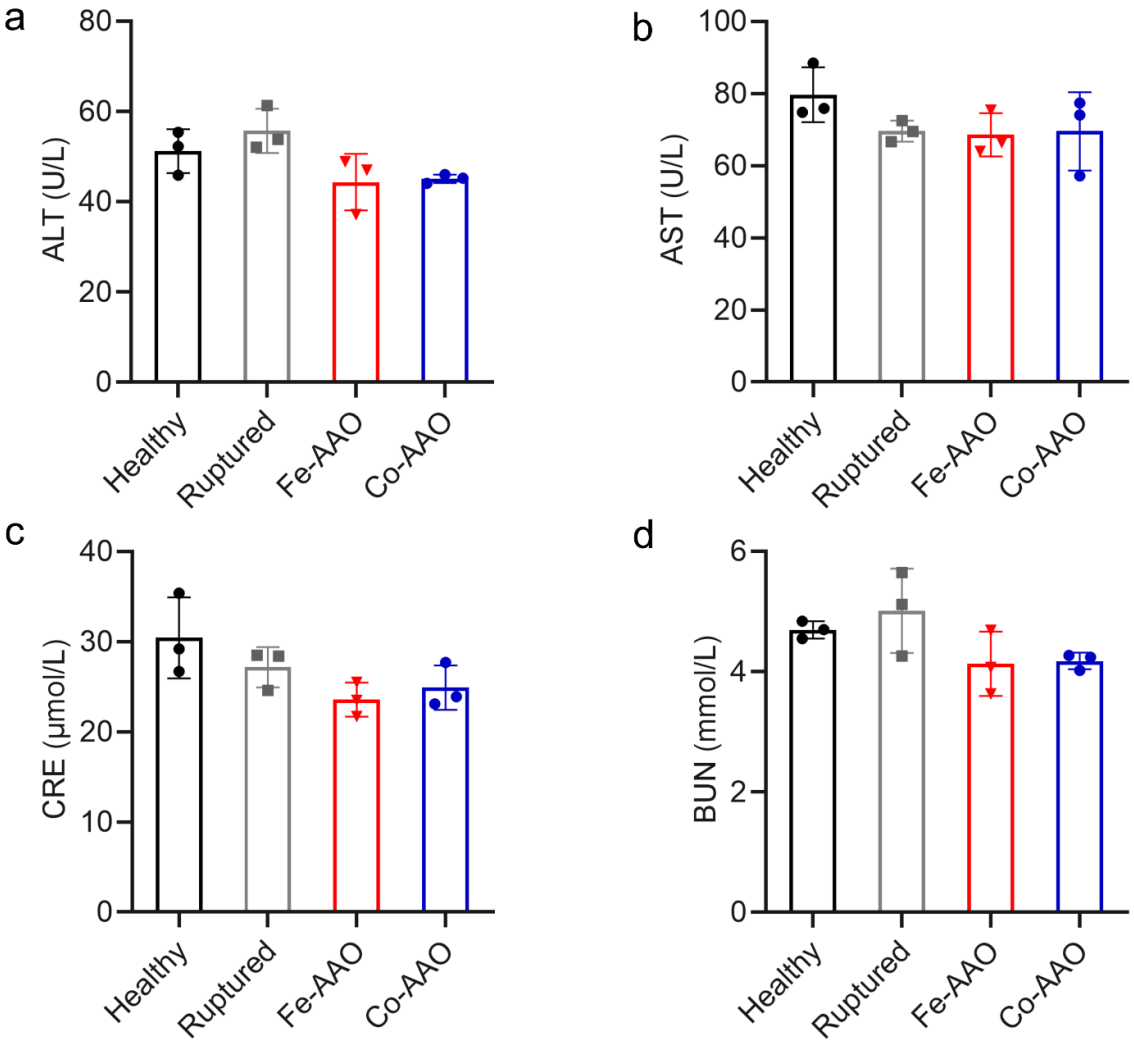

Figure S39. Serum biochemistry analysis of rats after repeated administration of FA-AAOs for 5 weeks (n = 3). ALT, alanine aminotransferase; AST, aspartate transaminase; CRE, creatinine; BUN, blood urea nitrogen. Data are presented as mean ± SD.

Supplementary Tables

Table S1. The contents of different types of coordination N for various samples (at %).

Sample	Pyridinic N/Fe-N	Pyrrolic N	Graphitic N	Quaternary N	Oxidized N
NC-AAO	57.13	13.62	16.08	3.36	9.81
Fe-AAO	54.71	13.51	17.26	3.07	11.44
Co-AAO	59.44	13.30	15.19	3.22	8.85
Ni-AAO	56.19	12.56	19.04	4.36	7.84

Table S2. EXAFS fitting parameters at the Fe, Co, and Ni *K*-edge for various samples.

Sample	Shell	*N*	*R*(Å)	$\sigma^2\times10^3$(Å^2)	ΔE_0 (eV)	*R* factor
Fe-AAO (S_0^2 = 0.70)	Fe-N	4.4	2.01	0.9	2.2	0.010
Co-AAO (S_0^2 = 0.74)	Co-N	4.1	1.92	8.6	-0.6	0.013
Ni-AAO (S_0^2 = 0.795)	Ni-N	4.0	1.85	0.006	-12.31	0.016

[a]*N*: coordination numbers; [b]*R*: bond distance; [c]σ^2: Debye-Waller factors; [d]ΔE_0: the inner potential correction. *R* factor: goodness of fit.

Table S3. Comparison of V_{max} and TON values with recently reported biocatalysts with CAT-like activity. TON=V_{max}/[E_0], where [E_0] is the mole concentration of metal in the whole nanomaterials.

Biocatalysts	v_{max} (μM s^{-1})	TON (s^{-1})	Ref.
Fe-AAO	117.65	57.29	*This work*
Co-AAO	66.23	25.21	*This work*
$Cu_{5.4}O$	15.04	0.2606	*Nat. Commun. 2020, 11, 2788.*
Cu NCs	418.41	0.23	*ACS Appl. Mater. Interfaces 2020, 12, 42521*
Co_3O_4 NPs	11.20	0.045	*J. Mol. Catal. A-Chem. 2013, 378, 30.*

Pero-nanozysome (Fe)	1.22	0.253	*Adv. Funct. Mater. 2020, 31, 2007130.*
Co_3O_4 nanoplates	2.38	0.0095	*Chem. Commun. 2019, 55, 159.*
Co_3O_4 nanocubes	1.23	0.005	
Co_3O_4 nanorods	1.88	0.0075	
Pd octahedrons	5.90	0.0252	
Mn_3O_4 Flower	122.17	1.8643	
Mn_3O_4 cubes	5.30	0.081	*Chem. Eur. J. 2018, 24, 8393.*
Mn_3O_4 polyhedron	5.80	0.0886	
Mn_3O_4 flakes	21.75	0.3323	
Co_3O_4 nanoflowers	1467.00	2.3584	*Biosens. Bioelectron. 2020, 165, 112342.*
$Au_{24}Cu_1$	5.83	1.945	*Nat. Commun. 2021, 12, 114.*
PVP-Ir NPs	540.00	2.1942	*ACS Appl. Mater. Interfaces 2015, 7, 8233.*
IrO_x NPs	5.64	0.0108	*Angew. Chem. Int. Ed. 2020, 59, 9491.*
Ft-Pt NPs	840.00	19.6638	*Biomaterials 32, 2011, 1611.*
RuTe NRs	0.9817	0.05	*ACS Nano 2020, 14, 4383.*
Co_3O_4 nanozyme	35.70	0.179	*Angew. Chem. Int. Ed. 2023, e202301879*
Co-N_4 SAzyme	37.20	37.2	
Co-N_3P SAzyme	31.50	78.8	
Co-N_3PS SAzyme	52.00	520	

Table S4. Comparison of V_{max} and TON with recently reported biocatalysts with GPx-like activity. TON=V_{max}/[E_0], where [E_0] is the mole concentration of metal in the whole nanomaterials.

Biocatalysts	**v_{max} (μM min^{-1})**	**TON (min^{-1})**	**Ref.**
Fe-AAO	39.70	3.8700	*This work*
Co-AAO	92.25	7.0200	*This work*
Co/PMCS	17.44	0.6976	*Angew. Chem. Int. Ed. 2020, 59, 5108.*
Mn_3O_4 nanoflowers	56.00	0.4278	*Angew. Chem. Int. Ed. 2017, 129, 14455.*
V_2O_5 nanowires	430.00	1.9580	*Nat. Commun. 2014, 5, 5301.*
V_2O_5 nanosheets	233.00	1.0610	*Angew. Chem. Int. Ed. 2018, 57, 4510.*
V_2O_5 nanoflowers	340.00	1.5482	

V_2O_5 nanospheres	458.00	2.0855	
V_2O_5 @PDA@MnO_2	88.00	0.3590	*Angew. Chem. Int. Ed. 2016, 55, 6646.*
Ebselen	187.80	2.3600	*Adv. Healthcare Mater. 2021, 10, 2001736.*
supramolecular nanocapsules	14.95	3.1600	*Chem. Commun. 2019, 55, 13820.*
CTMDs	2.41	0.5101	*Mater. Horiz. 2019, 6, 1682.*
Mn_3O_4 hexagonal plates	14.20	0.1085	*Chem. Eur. J. 2018, 24, 8393.*
Mn_3O_4 cubes	18.20	0.1390	
Mn_3O_4 polyhedron	16.90	0.1291	
Mn_3O_4 flakes	39.10	0.2987	

References:

1 J. Xu, X. Chen, L. Tan, C. Fu, M. Ahmed, J. Tian, J. Dou, Q. Zhou, X. Ren, Q. Wu, S. Tang, H. Zhou, X. Meng, J. Yu and P. Liang, *Nano Lett.*, 2019, **19**, 2914-2927.